Naval Research Laboratory

Stennis Space Center, MS 39529-5004

Implementation of Wetting and Drying in NCOM: Description and Validation Test Report

Paul J. Martin
Kacey L. Edwards
David A. Hebert
Rick A. Allard

Ocean Dynamics and Prediction Branch
Oceanography Division

August 4, 2015

REPORT DOCUMENTATION PAGE

1. REPORT DATE *(DD-MM-YYYY)* 04-08-2015	**2. REPORT TYPE** Memorandum Report	**3. DATES COVERED** *(From - To)*

4. TITLE AND SUBTITLE

Implementation of Wetting and Drying in NCOM: Description and Validation Test Report

5a. CONTRACT NUMBER

5b. GRANT NUMBER

5c. PROGRAM ELEMENT NUMBER
0602435N

6. AUTHOR(S)

Paul J. Martin, Kacey L. Edwards, David A. Hebert, and Rick A. Allard

5d. PROJECT NUMBER

5e. TASK NUMBER

5f. WORK UNIT NUMBER
73-6669-05-5

7. PERFORMING ORGANIZATION NAME(S) AND ADDRESS(ES)

Naval Research Laboratory
Oceanography Division
Stennis Space Center, MS 39529-5004

8. PERFORMING ORGANIZATION REPORT NUMBER

NRL/MR/7320--15-9573

9. SPONSORING / MONITORING AGENCY NAME(S) AND ADDRESS(ES)

Office of Naval Research
One Liberty Center
875 North Randolph Street, Suite 1425
Arlington, VA 22203-1995

10. SPONSOR / MONITOR'S ACRONYM(S)

ONR

11. SPONSOR / MONITOR'S REPORT NUMBER(S)

12. DISTRIBUTION / AVAILABILITY STATEMENT

Approved for public release; distribution is unlimited.

13. SUPPLEMENTARY NOTES

14. ABSTRACT

This report discusses the implementation and testing of wetting and drying (WAD) in the Navy Coastal Ocean Model (NCOM). Note that NCOM is run as a stand-alone ocean model and also as part of the Coupled Ocean/Atmosphere Mesoscale Prediction System (COAMPS), which provides for one- or two-way coupling among atmosphere, ocean, and wave models. The WAD in NCOM is tested by running simulations of (a) idealized experiments that have analytical solutions that can be compared against, (b) laboratory experiments that have observed results that can be compared against, (c) several coastal regions that have notable WAD areas, i.e., San Francisco Bay, Chesapeake Bay, and Cook Inlet in Alaska, and (d) Hurricane Ike, which caused extensive flooding along the Texas and Louisiana coasts in 2008. The pros and cons of the WAD scheme implemented in NCOM are discussed. This WAD scheme has the main advantages that it does not require any special modification of the bathymetry and is fairly robust. The main disadvantages of the WAD scheme are that additional calculations are required and the timestep may need to be decreased, both of which will increase the NCOM run time.

15. SUBJECT TERMS

Ocean modeling	Testing and validation	Turnagain Arm
Wetting and drying	Cook Inlet	Tidal flats

16. SECURITY CLASSIFICATION OF:

a. REPORT	b. ABSTRACT	c. THIS PAGE	**17. LIMITATION OF ABSTRACT**	**18. NUMBER OF PAGES**	**19a. NAME OF RESPONSIBLE PERSON** Paul Martin
Unclassified Unlimited	Unclassified Unlimited	Unclassified Unlimited	Unclassified Unlimited	54	**19b. TELEPHONE NUMBER** *(include area code)* (228) 688-5447

CONTENTS

IMPLEMENTATION OF WETTING AND DRYING IN NCOM: DESCRIPTION AND VALIDATION TEST REPORT

1. INTRODUCTION

Wetting and Drying (WAD) refers to the wetting or flooding of grid cells that were previously dry and the drying of grid cells that were previously wet (i.e., covered by water) during the temporal integration of an ocean or fluid-flow model. The Navy Coastal Ocean Model (NCOM) (Martin 2000, Morey et al. 2003, Barron et al. 2004) does not currently have a WAD capability; hence, grid cells cannot switch between being wet and dry, i.e., grid cells that are initially dry must stay dry and those that are initially wet must stay wet. There is no mechanism by which the WAD "front" between dry grid cells and wet grid cells can advance onto the dry cells when the sea-surface height (SSH) at the coast rises. Similarly, there is no mechanism by which the WAD front between the dry grid cells and the wet grid cells can retreat from the previously wet grid cells when the SSH at the coast falls.

The importance of WAD in a simulation depends both on the extent of the WAD areas in the domain covered by the ocean model and the grid resolution being used.

The rise of sea level at wet grid cells near the coast in NCOM does not cause any numerical problems; however, the inability of high water at the coast to flow inland over previously dry grid cells can reduce the accuracy of the prediction of SSH near the coast and does not allow prediction of the extent of inundation and flooding that might occur (Oey et al. 2007).

If the depth of the water at a shallow grid cell decreases to the extent that the grid cell drys out, i.e., the SSH drops to or below the ocean bottom at that grid cell, this currently causes a numerical instability in NCOM that will terminate the run. Hence, without a WAD capability, one is faced with setting a minimum depth at grid cells in shallow areas near the coast that is sufficiently deep that the grid cells will not dry out during a model run. This involves either setting a grid cell that is too shallow to be a land point, or increasing the depth of the grid cell sufficiently that it will not dry out. Hence, the fidelity of the bottom depth in these areas tends to be compromised, which can reduce the accuracy of the model predictions.

The maximum drop in sea level at points near a coast varies considerably and is mainly affected by the amplitude of the tides and the amount of "set down" of the SSH caused by the winds. The amount of set up or set down at the coast depends on the strength and direction of the winds and the shape of the local coastline and bathymetry. For example, the gradient of the SSH between the mouth and head of a bay is approximately proportional to the distance between the mouth and the head of the bay and the magnitude of the wind stress and is inversely proportional to the water depth. Thus, the total set up or set down at the head of the bay increases when the wind stress

and the length of the bay increase and when the water depth is reduced. Hence, a strong wind blowing away from the head of a long, shallow bay towards the mouth of the bay is a situation that can lead to a significant drop in the SSH at the head of the bay and may lead to drying of grid cells near the head of the bay if the grid cells are sufficiently shallow.

In this report, a distinction is made between "extensive" and "occasional" WAD. Extensive WAD occurs when there are extensive areas where WAD is regularly occurring during the model run. This typically occurs when relatively high horizontal grid resolution is being used and there are relatively low-lying land areas and/or shallow sea areas near the coast and the tides are relatively large so that WAD is frequently occurring. A prime example of such an area is Cook Inlet, Alaska, which has a tidal range of over 10 m near its head and contains large areas of tidal mud flats that are uncovered during low tides and covered up during high tides (Oey et al. 2007).

Occasional WAD occurs when a domain does not have extensive WAD areas relative to the grid resolution being used, and drying of grid cells occurs only occasionally, e.g., due to the tides or to set down of the SSH at the coast or at the head of a long, shallow bay due to offshore winds or a combination of both. In such cases, a WAD capability allows the ocean model to continue running smoothly during periods when one or more relatively shallow grid cells have dried out.

This report is organized as follows. The implementation of WAD in NCOM is discussed in Section 2. Tests of the WAD scheme are presented in Section 3. Some limitations of the WAD scheme implemented in NCOM are discussed in Section 4. A summary of the report is presented in Section 5.

2. IMPLEMENTATION OF WAD IN NCOM

2.1 Scheme used to implement WAD in POM by Leo Oey

WAD was fairly recently implemented in the Princeton Ocean Model (POM) (Blumberg and Mellor 1987) by Leo Oey (Oey 2005, 2006) using a relatively simple scheme, and the WAD implemented in NCOM is, in part, based on the methods used by Oey. The key part of the implementation of WAD in POM occurs in the solution of POM's barotropic or free-surface mode, which involves the solution of the equations for the update of the SSH ζ and the barotropic transports U and V (the barotropic transport is the water depth times the depth-averaged velocity). These are similar to the barotropic equations for a single-layer, shallow-water model. The depth-integrated continuity equation can be written as

$$\frac{\partial \zeta}{\partial t} = -\frac{\partial U}{\partial x} - \frac{\partial V}{\partial y} + Q, \tag{1}$$

and the depth-integrated momentum equations can be written as

$$\frac{\partial U}{\partial t} = -gD\frac{\partial \zeta}{\partial x} + F_u, \tag{2}$$

$$\frac{\partial V}{\partial t} = -gD\frac{\partial \zeta}{\partial y} + F_v, \tag{3}$$

where t is the time, x and y are the horizontal coordinates, Q is a depth-integrated volume source term, g is the acceleration of gravity, D is the dynamic water depth (i.e., which changes in time

due to changes in the SSH), and F_u and F_v represent the vertical integral of the forcing terms from the baroclinic momentum equations being applied to the barotropic equations.

At this point it is useful to define the static bottom depth H, which is the depth from the static (fixed) surface at $z = 0$ to the sea bottom. This static bottom depth H is defined to be positive upward in both POM and NCOM, hence, its value is negative at sea points where the bottom lies below $z = 0$ and is positive at points where the bottom lies above $z = 0$. The dynamic water depth D is the total thickness of the water column between the bottom and the free surface ζ. The dynamic water depth is computed as $D = \zeta - H$ and should always be ≥ 0.

POM solves its barotropic equations using what is referred to as a split-explicit scheme whereby these equations are solved explicitly with a smaller time step than the rest of POM's equations, i.e., the equations for the baroclinic (depth-dependent) velocities and the temperature and salinity fields. Note that POM also includes barotropic (i.e., depth-integrated) forms of the horizontal advection and Coriolis terms in its depth-integrated momentum equations, which are updated during the time integration of the barotropic mode. Since these terms are not essential for the discussion presented here, they have not been explicitly included in Eq. (2)–(3).

The temporal numerical scheme used to update the barotropic equations explicitly in POM, which is the leapfrog time-differencing scheme, can be written for the depth-integrated continuity equation as

$$\zeta^{n+1} = \zeta^{n-1} + 2\Delta t[-(\delta_x(\Delta y_u U^n)/\Delta x + \delta_y(\Delta x_v V^n)/\Delta y) + Q^n] \tag{4}$$

and for the depth-integrated momentum equations as

$$U^{n+1} = U^{n-1} + 2\Delta t[-gD_u\delta_x\zeta^n/\Delta x_u + F_u^n] \tag{5}$$

$$V^{n+1} = V^{n-1} + 2\Delta t[-gD_v\delta_y\zeta^n/\Delta y_v + F_v^n] \tag{6}$$

where the superscripts $n+1$, n, and $n-1$ denote values of the prognostic variables at the new, current, and previous time levels of the leapfrog time-differencing scheme, respectively, the subscripts u and v denote values at the u and v points, respectively (both POM and NCOM use an Arakawa C-type grid where the velocities are defined at the center of the faces of the main grid cells), Δt denotes the time step, Δx and Δy denote grid spacings in the x and y directions, respectively, and the symbols δ_x and δ_y denote taking differences in the x and y directions, respectively.

What makes the update of these equations explicit is that everything that is needed to compute the new values of ζ, U, and V, which is on the right-hand-side (RHS) of Eq. (4)–(6), is known, and so the new values can be easily calculated.

These explicit equations must be solved with a small time step because, for explicit equations, the time step must be smaller than the time required for the fastest propagating waves or signals described by the equations to travel the length of a single grid cell. For these barotropic equations, the fastest signals are the surface gravity waves, which have a speed of $c_{sgw} = (gD)^{1/2}$. In the deep ocean, i.e., where the depth is on the order of 4000 m or more, the speed of the surface gravity waves is greater than 200 m/s. By contrast, the fastest signals in the baroclinic equations are the speeds of the internal gravity waves and ocean currents, which are generally not much more than 3–4 m/s and are usually somewhat less.

Oey's WAD method is the following: (1) All grid cells that are "wettable", i.e., either can be wet or are wet, always remain in the "computational domain" and are (usually) always covered by a thin film of water. (Grid cells not defined to be in the computational domain are considered to be land that can never be wet.) (2) After the new barotropic variables (ζ, U, and V) are computed, if the new water depth D in any grid cell is less than some minimum specified depth D_{min} (e.g., $D_{min} = 0.1$ m), then the transports directed "out" of those grid cells are set to zero. (3) On the next time step, step (2) is repeated.

Because the new transports computed by Eq. (5)–(6) will be used to update the SSH on the next time step using Eq. (4), Oey's step (2) insures that at grid cells with a water depth less than D_{min}, the water depth will not drop any further.

Oey's step (2) presumes that the water depth D in a grid cell will not drop from above D_{min} to zero or below in a single time step. Because of the small time step used for the barotropic equations, and depending on the value of D_{min}, this is usually the case. However, even with the small time steps typically used with POM's split-explicit free surface, it could possibly happen that D becomes ≤ 0. If this does happen, then either D_{min} must be increased, or the time step being used for the barotropic equations must be reduced.

A situation that increases the likelihood of the water depth in a grid cell dropping more than D_{min} and drying out in a single barotropic time step is having a shallow grid cell that can dry out next to a relatively deep grid cell. On a typical sigma coordinate grid, the bottom depth at the velocity point on the interface between two grid cells is the mean of the bottom depth of the two grid cells. Hence, if one of the grid cells is relatively deep, the depth at the velocity point will also be relatively deep, and the transport between the two grid cells, which is proportional to the area of the grid-cell face that the two grid cells share, could potentially be fairly large and, hence, more likely to dry out the shallow grid cell during a time step.

One strategy to reduce the likelihood of this happening is to avoid having a very deep grid cell next to a shallow grid cell that can dry out. Another strategy is to define the depth of the velocity point between the two grid cells to be equal to that of the shallower of the two grid cells rather than the mean depth of the two grid cells. Using either of these strategies will tend to reduce the rate of transport of water out of the shallow grid cell during a time step and, hence, tend to reduce the rate at which it dries out. Note that if such a modification of the bottom depth at velocity points was being used, it would only need to be done in shallow areas where WAD can occur.

An advantage of the WAD scheme implemented by Oey (2005, 2006) is that not many additional changes to POM were required to adapt the rest of the model for WAD. The main additional changes that are required for WAD are as follows. (1) The baroclinic velocities are set to zero at the boundaries of grid cells that have "dried out", i.e., where $D < D_{min}$. (2) Static bottom depths H that are greater than zero, i.e., at what would normally be land areas, need to be allowed for. (3) Calculations that depend on the thickness or depth of a grid cell, such as the bottom drag coefficient and the solar extinction, may need to be updated more frequently, since the values at shallow grid cells, especially those that are beginning to flood or are near to drying, can undergo relatively large changes in a short period of time.

4

2.2 Implementation of WAD in NCOM's Explicit Barotropic Solver

The WAD scheme of Oey (2005, 2006), described in the previous section, was implemented in NCOM's explicit barotropic solver for the new SSH and barotropic transports. This routine is used to provide a "preliminary" estimate of the new SSH when NCOM is run in the usual way using an implicit solution for the new SSH, and is also used to compute the new SSH and barotropic transports explicitly when NCOM is run in fully explicit mode using the same (small) time step for both the barotropic and baroclinic equations.

Note that NCOM is not usually run in fully explicit mode because, using the small time step that is needed to explicitly solve the barotropic equations to solve the baroclinic equations results in NCOM taking a great deal of time to run, i.e., the size of the time step required to solve the barotropic equations explicitly can be more than 50 times smaller than that required to solve the baroclinic equations if the model domain contains deep areas. However, this option is provided for testing purposes, or in case a fully explicit solution is desired, e.g., for comparison with the implicit solution for the new SSH.

2.3 Implementation of WAD in NCOM's Implicit Barotropic Solver

To implement WAD with NCOM's implicit solution of the barotropic equations (Martin 2000), a variation of Oey's WAD scheme is used. After the new SSH is computed (using an iterative solver), the new water depth in each grid cell is inspected and, for grid cells whose depths have fallen below a prescribed minimum D_{min}, the volume fluxes at cell faces that are directed "out" of the drying grid cells are set to zero by setting the solver coefficient for those grid-cell faces to zero, and then the free-surface solver is rerun.

This iterative procedure is repeated until convergence occurs, i.e., until no grid-cell depths drop below D_{min} or the maximum difference in the SSH from the calculation of the SSH on the previous iteration falls below a small prescribed value (currently set to 10^{-6} m). Note that volume fluxes set to zero on earlier iterations during the current time step remain set to zero during later iterations. However, as with Leo Oey's scheme in POM, everything starts over again on the next time step, i.e., all the grid cells in the "computational domain" are included in the initial calculation of the new SSH on the next time step. This allows "dry" grid cells to readily flood when the SSH in the adjoining grid cells begins to rise.

Note that, with this scheme, the water depth D at grid cells within the computational domain is not allowed to fall much below the minimum specified depth D_{min}. For this reason, the scheme has proven to be fairly robust in the testing done to date.

Since the water depth D at grid cells within the computational domain cannot fall much below the value specified for D_{min}, one could consider making D_{min} fairly small, so that the layer of water left behind in "dry" areas will tend to be relatively shallow. However, a drawback of this is that, as the water depths become very shallow, larger velocities may occur in the areas where the grid cells are shallow, which would increase the possibility of violating the Courant-Friedrichs-Lewy (CFL) limitation for explicit numerical advection, which is that the advection of a field cannot exceed the width (or thickness for vertical advection) of a grid cell in a single time step. We typically set the value for D_{min} in our coastal simulations to 10 cm. Even with this value of D_{min}, the time step for

simulations that include WAD sometimes has to be reduced to prevent violation of the advective CFL limitation in the WAD areas.

Note that reduction of the time step is not always needed when WAD is added, or when using WAD and the value of D_{min} is reduced, but if the time step does have to be reduced, it can result in significant additional cost for the simulation, e.g., if the time step is halved, the time required for the simulation will be almost doubled. This is significantly more than the cost of just the additional calculations required for WAD, which is typically less than 20%. We have conducted WAD simulations with values of D_{min} of 10, 5, 2, 1, and 0.1 cm, and these have run robustly as long as the time step was reduced sufficiently to avoid exceeding the advective CFL limitation. Finding the "maximum" time step that will work for a given domain or a particular situation usually takes some trial and error, though this is also the case for simulations without WAD.

2.4 General Modifications of NCOM for WAD

At grid-cell faces at which the barotropic transport is set to zero during the calculation of the barotropic equations (i.e., to prevent the water depth D at a grid cell from dropping below D_{min}), the baroclinic velocities are also set to zero.

Without WAD, the static bottom depth H at active (sea) grid cells in the computational domain is always less than zero. However, with WAD the static bottom depth at an active grid cell can be set to be ≥ 0. Hence, locations in the NCOM computer code where the use of a value of $H \geq 0$ would generate unphysical values must be modified. This is typically done by setting a maximum allowable value for H that is less than zero (e.g., -0.1 m) to be used in such calculations.

Some parameterizations in NCOM that depend on the layer depth or thickness, such as the calculation of the the solar extinction and the bottom drag coefficient, are usually computed only at the start of a model run based on the static layer depths or thicknesses. However, with WAD, the calculation of the solar extinction and the bottom drag coefficient with the static layer depths or thicknesses will be inaccurate and/or ill-defined in WAD areas, and both the solar extinction and the bottom drag coefficient can change significantly at grid cells undergoing WAD. Hence, options are provided to update these quantities each time step using the current dynamic layer depths and thicknesses, which change on the sigma-coordinate grid with changes in the SSH. Note that, previously, calculation of the bottom drag coefficient each time step using the dynamic bottom-layer thickness was provided when ocean-wave coupling was being used to allow for the enhancement of the bottom drag coefficient by the wave motion near the bottom (i.e., in the wave-bottom boundary layer), which has a large variation in time as the waves change.

For WAD a new input flag, *indwad*, is provided for NCOM to define whether WAD will be computed during the run. This flag is set to zero if there is no WAD (this is the default value) and must be set to a value of one if WAD is to be accounted for. Another new input flag, *iwadiag*, can be used to increase the amount of diagnostic printout associated with the WAD. The default value of *iwadiag* is zero, and larger values increase the amount of diagnostic output. This output can be used to help diagnose any problems associated with the WAD and to check the conservation of the WAD scheme.

The value of D_{min} can be specified as an input to NCOM if a value other than the default value of 0.1 m is desired. However, note that within the NCOM code and within NCOM's input

parameter files, this parameter is called D_{wet}, which was considered to be a more unique and representative name.

When computing the new value of the SSH and checking for values of $D < D_{min}$ for WAD, it is not necessary to check points where the value of D is relatively large that are unlikely to dry out during that time step. Hence, the first time this check is being conducted on a particular time step, NCOM makes a list of the grid cells within the computational domain where D is less than a specified minimum value D_{wad}, and only these points are checked for $D < D_{min}$ on that time step. This reduces the amount of time that NCOM spends doing this checking. The default value of D_{wad} is set to 4 m, but a different value can be specified as an input parameter. Experience has shown that D_{wad} needs to be set to a value on the order of the maximum tidal amplitude within the domain, or on the order of the maximum wind setup or set down, whichever is greater. For example, a value of $D_{wad} = 3$ m was found to be adequate for simulations of the tide in Cook Inlet where the maximum tidal amplitude is about 5 m. If D_{wad} is set too small, the calculation of the new SSH may not converge and the NCOM simulation will terminate. Hence, if an NCOM simulation terminates during the calculation of WAD during the update of the SSH, it may be that the value of D_{wad} being used is too small.

When WAD is being used, the surface values of the land-sea mask, which define which grid cells are inside and which are outside the computational domain, can no longer easily be determined from the two-dimensional (2D) array of static bottom depths H. For this reason, a 2D, surface, land-sea mask is now added to the NCOM input horizontal grid file during the setup of an NCOM run. This 2D land-sea mask becomes the seventh 2D record within the horizontal grid file, and follows the six previous 2D arrays in this file containing: (1) longitude, (2) latitude, (3) grid spacing in x, (4) grid spacing in y, (5) static bottom depth H at sea (i.e., all wettable) points, and (6) the angle of the grid with respect to the local longitude and latitude. When NCOM starts up, the land-sea mask is read from the horizontal grid file if WAD is being used. If WAD is not being used, the land-sea mask is computed from the bottom depth array as was done before without WAD, i.e., points with $H < 0$ are defined as sea points and are inside the computational domain and all others are defined as land points and are outside the computational domain. This (and the default value of input parameter *indwad* being zero) helps maintain backward compatability for the updated NCOM code that includes WAD, with older sets of NCOM input files that were set up before the WAD was implemented.

2.5 Bottom drag

The bottom drag plays an important role in the dynamics of WAD, i.e., very shallow flows in WAD areas are often mainly determined by a balance between the surface pressure gradient due to the slope of the SSH and the bottom drag. Hence, the calculation of the bottom drag and the specification of the bottom drag coefficient is an important aspect of WAD simulations. For these reasons, the bottom drag parameterization used in NCOM will be discussed here.

NCOM uses a quadratic parameterization of the bottom drag (Martin 2000); hence, the bottom stress terms on the RHS of NCOM's u and v momentum equations are $-C_b u|\mathbf{v}|$ and $-C_b v|\mathbf{v}|$, respectively, where C_b is the bottom drag coefficient, and u and v are the two components of and $|\mathbf{v}|$ is the magnitude of the horizontal velocity in the bottom layer.

The value of the bottom drag coefficient C_b used in NCOM can be specified, or can be calculated

in terms of the bottom layer thickness Δz_b and the bottom roughness z_o as

$$C_b = \max \left[\left(\frac{\kappa}{\ln \left[1 + \frac{\Delta z_b}{2z_o} \right]} \right)^2 , C_{b_{min}} \right] , \tag{7}$$

where $\kappa = 0.4$ is von Karman's constant, and $C_{b_{min}}$ is a minimum allowed value for C_b. If the bottom roughness z_o is set to zero, the bottom drag is just set equal to $C_{b_{min}}$. This expression for C_b assumes (i.e., is derived assuming) a logarithmic boundary layer velocity profile near the bottom. For a flow being treated as a single layer, the value of Δz_b in Eq. (7) is just the water depth.

A commonly used alternative for computing the drag on a flow, which is frequently used in engineering, is the Manning formulation. With the Manning formulation, the bottom drag coefficient for a shallow-water flow that is being treated as a single-layer flow is computed as

$$C_b = gn^2/D^{1/3} \tag{8}$$

where g is the gravitational constant, D is the water depth, and n is the Manning roughness coefficient, which depends on the characteristics, e.g., the roughness, of the bottom. Since the bottom drag coefficient C_b is dimensionless, the Manning roughness coefficient has units of $s/m^{1/3}$. Values of the Manning roughness coefficient can be found in the literature for a wide range of material and bottom types.

The use of the Manning formulation for the bottom drag is not currently provided as an option in NCOM. However, in both of the bottom drag coefficient formulations described by Eq. (7) and (8), the bottom drag coefficient increases as the water depth decreases, though at somewhat difference rates. Hence, when describing a single-layer flow, an approximate correspondence can be found between the bottom roughness z_o and the Manning friction coefficient n for a specific, limited range of water depths.

2.6 Pre- and Post-Processing Modifications for WAD

Calculations used in pre-processing (i.e., setting up) an NCOM simulation as well as post-processing of NCOM output must allow for the use of WAD if there are values of the static bottom depth $H \geq 0$ within the computational domain.

Setting up the bathymetry for a domain involves a number of procedures that are sensitive to the value of H being ≥ 0. These procedures include: calculation of the land-sea mask, smoothing/filtering of the bathymetry, calculation of steep bottom slopes, reduction of steep bottom slopes, and the determination of a single, main, contiguous, computational domain.

For all of these procedures, values of $H \geq 0$ can be accommodated by defining (a) a minimum elevation for land points that are defined to be outside the computational domain and/or (b) a reference height that is above the highest allowable elevation of grid cells that are defined to be within the computational domain. Setting a minimum elevation to define land points that are outside the computational domain provides a simple rule for computing the land-sea mask that defines the computational domain. Alternatively, the rule(s) used for defining the computational domain can vary spatially, but this is more complex to implement. Defining a reference height

for the grid cells within the computational domain is useful for providing a reference height for computing and adjusting bottom slopes. Note that smoothing bottom depths and reducing steep slopes within and adjacent to WAD areas can increase the robustness of the WAD calculations within an NCOM simulation and may reduce the need to decrease the time step to avoid violating the advective CFL constraints.

As noted previously, when providing for WAD, NCOM tries to maintain a minimum water depth D_{min} at all grid cells within the computational domain. Consequently, when the SSH (ζ) is initialized in an NCOM setup program, the SSH at grid cells within the computational domain can be defined so that the initial dynamic water depth $D = \zeta - H$ is $\geq D_{min}$. However, NCOM can adjust if a different value of D_{min} was used to define the initial SSH as long as $D \geq 0$.

For convenience, pre- and post-processing of NCOM input and output frequently involves calculating a three-dimensional (3D) array of static or dynamic grid-cell interface depths. Such an array can be used to define the vertical structure of most grids, including NCOM's sigma, sigma/z-level, and generalized vertical coordinate grids, and is useful for computing or accessing depth-dependent quantities and values from data bases for model setup and for processing model output. In the case where WAD is being used and there are values of $H \geq 0$, it is usually sufficiently accurate for most pre- and post-processing needs to define a 3D array of static interface depths in which the maximum (shallowest) layer depths are defined to be small, negative values increasing (however slightly) upwards towards a static free surface at zero elevation, so that the depths computed from this array of interface depths will always be negative and the computed layer thicknesses will always be positive (i.e., as for the case when WAD is not being used). This is because many of the data bases and procedures used in pre- and post-processing are expecting a value of the depth at a sea point that is ≤ 0.

3. WAD TEST CASES

3.1 Initial Gaussian Bump Symmetry Test

NCOM is written so as to be able to maintain perfect symmetry for horizontally symmetric problems. This is accomplished by grouping terms in the calculations in NCOM to maintain horizontal symmetry, e.g., if differencing the horizontal fluxes on the six faces of a grid cell, the separate differences in x, y, and z are computed first, then the x and y flux differences are combined, and then the flux difference in z is added. Such grouping of the calculations makes use of the fact that, in most computers, the sum or product of two quantities gives the same result independent of which quantity appears first in the compute instruction. However, the sum or product of three or more quantities will vary, due to roundoff error, depending on the order in which the calculation is performed.

Checks for the horizontal symmetry of the NCOM solutions for horizontally symmetric problems provides a very useful check on the coding and is especially useful for detecting loop-indexing errors. This is especially useful for the NCOM code, since the bulk of the calculations in NCOM are done in a horizontally asymmetric fashion, i.e., the update of the 3D momentum fields and the 3D scalar and turbulence fields is done by proceeding through the model domain in single x-z slices. This is done to improve the efficiency of the use of high-speed cache memory when there are a lot of grid points being computed on each processor. By only computing a single, 2D, x-z

slice at a time (rather than the full 3D grid), there is greater likelihood that more calculations can be done with the variables being held within the high-speed cache before they are flushed out by the need to access variables not currently in the high-speed cache. In summary, the asymmetric way in which most of NCOM's updates proceed through the model domain makes for efficient use of high-speed cache, but provides a lot of potential for coding errors. Hence, a test for horizontal symmetry is usually the first test that is performed on NCOM after extensive coding changes have been made.

The typical horizontal symmetry problem that is used is set up within a square domain. The lateral boundaries may be open or closed (usually, both of these situations are tested). The initial condition is taken to be a Gaussian-shaped bump in the SSH, centered within the domain. A similar type of symmetric bump is usually incorporated in the initial salinity field. Hence, when the simulation is started, both the SSH bump and the internal salinity bump propagate outwards towards the edges of the domain as external and internal gravity waves, and either pass through the open boundaries, or are reflected at the boundaries if they are closed. Typically, as much variability as possible is added to this problem in order to make the test as thorough as possible, the only limitation being that what is added is added in a horizontally symmetric way, e.g., spatially-variable horizontal grid spacing, spatially-variable bathymetry, atmospheric forcing, and river inflows. The resulting solutions should have an eight-fold symmetry when the Coriolis term is taken to be zero, and a four-fold symmetry if the Coriolis term is taken to be constant. NCOM provides subroutines that automatically check for these symmetries when this test is being conducted.

To test NCOM's WAD scheme, WAD areas were added to the grid in a symmetric fashion to be exposed or submerged as the initial Gaussian SSH bump propagates outward from the center of the grid. Note that our initial symmetry tests of the WAD scheme did expose some problems with the changes that had been made to incorporate the WAD (i.e., as it has many times in the past, the symmetry test proved its usefulness). After correction of these problems, the solutions were symmetric.

Note that in recent years, we have found that successful conduct of the symmetry tests requires that the NCOM code be compiled at a fairly low level of optimization. It appears that, at high optimization levels, the parentheses employed in the NCOM code to specify the order of the arithmetic operations are sometimes ignored/over-ruled by the aggressive optimization of the compiler. When this happens, the solutions still tend to be "correct", i.e., within the limits of computer roundoff error, but may not be perfectly symmetric.

3.2 Sloshing around a Parabolic-Shaped Basin

This test problem was used by Guan et al. (2013) to test a WAD scheme. Note that this test problem was originally described by Thacker (1981). The test involves the propagation of a planar surface wave around in a parabolic-shaped basin. WAD occurs at the edge of the basin as the surface wave propagates along the edge of the basin. The shape of the basin is given by

$$h(x,y) = \frac{h_0}{a^2}(x^2 + y^2), \tag{9}$$

where h is the bottom depth relative to a zero reference level, $h_0 = -10$ m is the water depth at the center of the basin, $a = 8025.5$ m is the radius of the basin at zero elevation, and x and y are

10

the horizontal coordinates. Note that h was defined to be positive downward in Guan et al. (2013), but has been defined to be positive upward here to be consistent with the sign convention used in NCOM.

This problem has an exact analytical solution given by

$$\zeta(x, y, t) = -\frac{Ah_0}{a^2}[2x\cos(\omega t) + 2y\sin(\omega t) - A] - h_0, \tag{10}$$

$$u(t) = -A\omega\sin(\omega t), \tag{11}$$

$$v(t) = -A\omega\cos(\omega t), \tag{12}$$

where ζ is the SSH, $A = a/10 = 802.55$ m is a constant that determines the amplitude of the motion, $\omega = (2gh_0)^{0.5}/a = 2\pi/T$ is the rotational frequency, $g = 9.81$ m^2/s is the acceleration of gravity, $T = 3600$ s is the period of rotation, t is the time in s, and u and v are the components of the velocity in the x and y directions, respectively. Note that the velocity is always at a right angle to the slope of the SSH, and the sign used in Eq. (12) for the v velocity determines the direction of rotation, which will be clockwise in this case.

As in Guan et al. (2013), the problem is solved in a 20×20 km domain with a 200×200 grid and a uniform horizontal grid resolution of 100 m. Only one layer is used in the vertical. The initial SSH and velocities are as described by Eq. (10)–(12) at time $t = 0$. The bottom drag is set to zero. The time step is 10 s. The third-order upwind scheme (Holland 1998) is used for momentum advection in the NCOM simulation.

We initially ran the simulation with a minimum water depth D_{min} within the computational domain of 0.1 m. However, the rotation speed, which should be one revolution per hour, was about 0.8% fast. Reducing the minimum water depth D_{min} to 0.01 m reduced the rotation speed error to about 0.07%. We also initially ran with a small but non zero value of the bottom drag coefficient, with a maximum value of 0.000042; however, this resulted in damping of the solution of about 2% per rotation. Setting the bottom drag to zero, which it should be for this idealized problem, noticeably reduced the damping. No reduction of the time step was needed to incorporate these changes, though reducing the value of D_{min} from 0.1 to 0.01 m increased the maximum value of the horizontal advective CFL values from 0.31 to 0.45 (the numerical advection is stable for maximum advective CFL values below one).

Figure 1 shows a comparison of the SSH simulated by the model with the SSH computed from the analytical solution in Eq. (10) along a line through the middle of the basin at $y = 0$ at times of 1, 5.2, 5.5, and 6 h (the period of rotation is 1 h). The model solution still shows good agreement with the analytical solution after 6 h.

Some aspects of the implementation of WAD illustrated by this test case are: conservation of volume, accurate simulation of the speed of rotation of the wave around the basin, and negligible damping of the amplitude of the wave (when the bottom drag is set to zero).
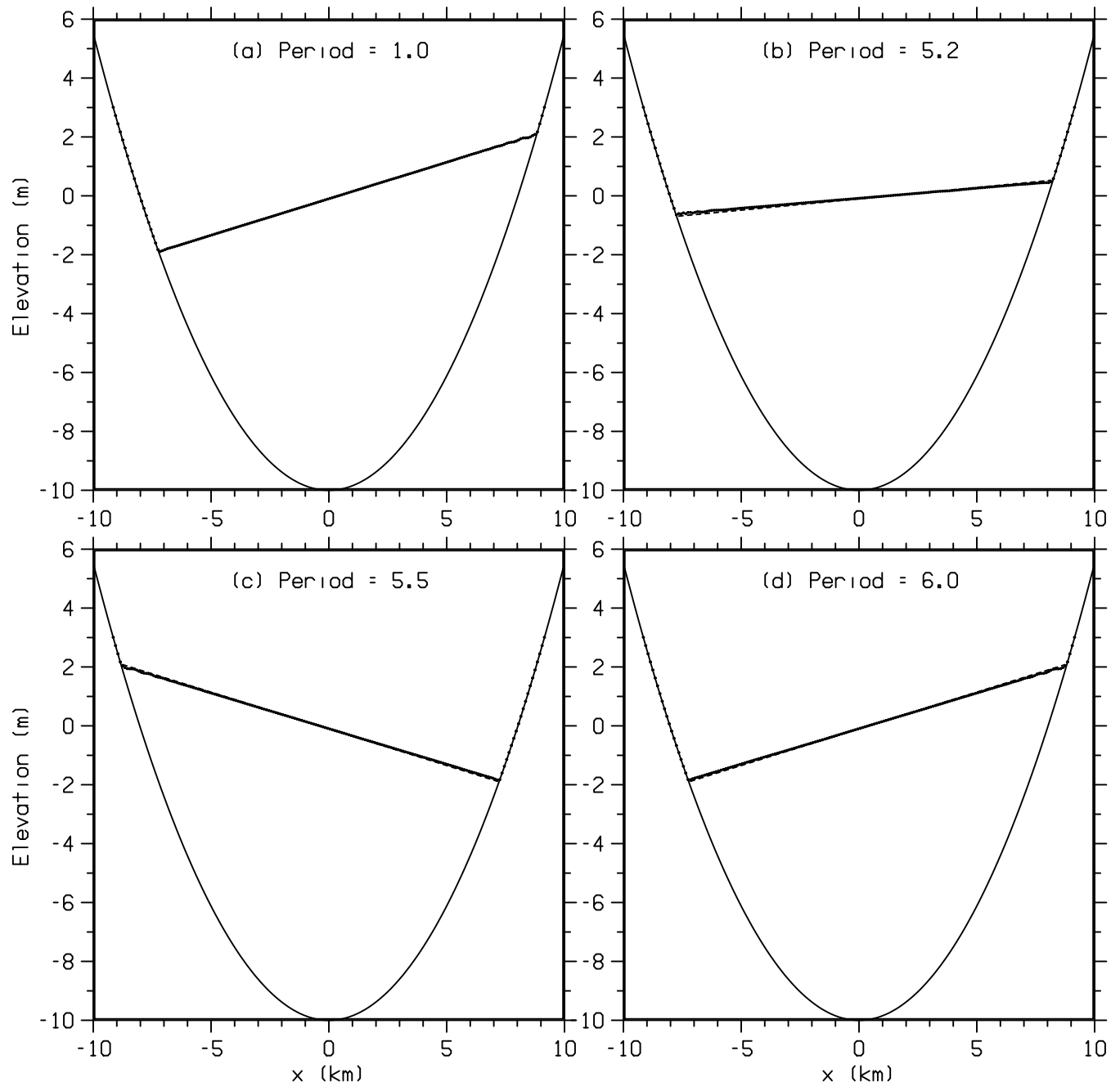
Fig. 1 — Comparison of model-simulated SSH (dots) with analytical solution (dashed line) at $y = 0$ after (a) 1 period, (b) 5.2 periods, (c) 5.5 periods, and (d) 6 periods.
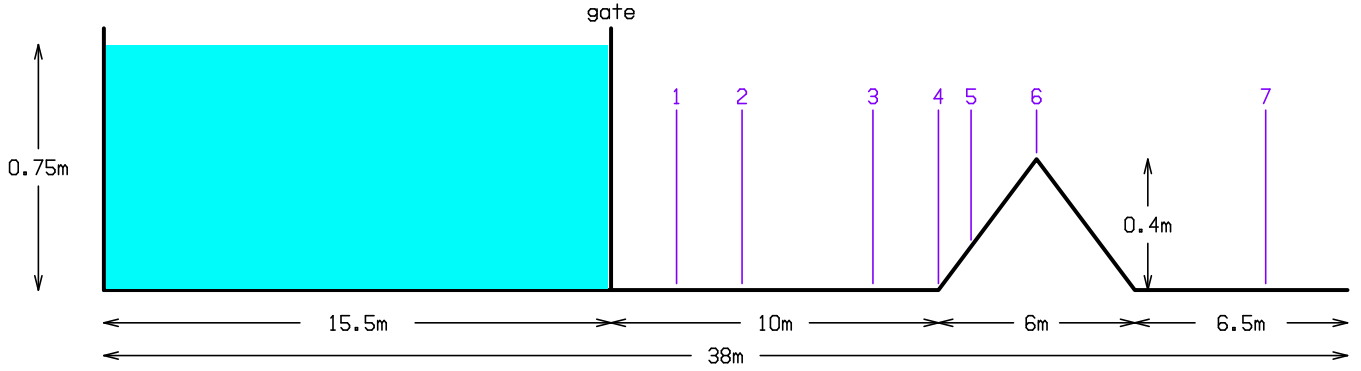
Fig. 2 — Setup and dimensions for laboratory experiment for a dam-break flow over a triangular bump.

3.3 Dam Break Flow over a Triangular Bump

This test case involves the simulation of a WAD laboratory experiment that was conducted by the Universite Libre de Bruxelles and the Laboratoire de Recherches Hydrauliques (Chatlet), Belgium under the supervision of Professor J.M. Hiver (Alcruco and Soares Frazao 1999). The experiment was conducted to provide data for testing WAD in dam-break and inundation numerical models. The results from this laboratory experiment have been used for testing numerical models by a number of investigators, e.g., Alcrudo (1999), Benkhaldoun et al. (1999), Garcia-Navarro and Brufau (1999), Brufau et al. (2002), Cozzolino et al. (2006), Loukili and Soulaimani (2007), Liang and Marche (2009), Singh et al. (2011), Guan et al. (2013), and Khan and Lai (2014).

The setup of the experiment is illustrated in Fig. 2. Water contained within a holding tank on the left end of a channel is suddenly released by opening a gate at the front (i.e., on the right end) of the tank. After it is released, the water flows down the channel and some of the water flows over a triangular-shaped bump. During the experiment, the surface elevation was measured at seven locations along the channel. These SSH measurement locations are shown in Fig. 2 (denoted by the purple lines) and are at distances of 2, 4, 8, 10, 11, 13, and 20 m from the front of the tank.

NCOM was set up for this test case with a horizontal grid resolution of 0.04 m. Beyond the end of the experimental setup shown in Fig. 2, a catch basin of length 5 m was used to collect the water flowing out the right end of the channel. Hence, the total length of the domain used for the NCOM simulation, including the catch basin, was 43 m. Only 3 points were used in the cross-channel direction, with just the middle point being a water point and the first and third points being land outside the computational domain with free-slip land-sea boundaries. (Alternatively, periodic boundaries could have been used in the cross-channel direction, in which case the results would have been the same, or the true width of the channel in the y-direction along with the side boundaries could have been simulated.) Only a single layer was used in the vertical. The third-order upwind scheme was used for momentum advection. Quadratic bottom drag was used with a bottom roughness of 3.5×10^{-5} m and a minimum value of the bottom drag coefficient of 0.0001 (see Section 2.5). This bottom roughness corresponds approximately to a Manning roughness coefficient of 0.0125 s/m$^{1/3}$, which is the value specified for the experimental setup by Alcrudo and Soares

13

Frazao (1999). These give values for the bottom drag coefficient of 0.0023 for a water depth of 0.3 m. Runs were made with the minimum water depth D_{min} set to 0.1, 0.01, and 0.001 m. Using smaller values of D_{min} reduced the speed of the wetting front and improved agreement with the observations. The results shown are for $D_{min} = 0.001$ m. The time step used was 0.002 s and output from the model simulation was saved at 0.1-s intervals.

Figure 3 shows the SSH from the model simulation at 5-s intervals from 0 to 85 s. At 5 s, the released water has reached the top of the triangular bump. Some of the water passes over the bump and some is reflected back towards the tank. At 30 s, the wave reflected back towards the tank by the triangular bump has been reflected by the wall on the left side of the tank and has started propagating back towards the bump. This sequence is repeated several times, i.e., some water passes over the triangular bump and a wave is reflected by the bump back towards the tank and is then reflected by the back wall of the tank back towards the triangular bump. Three of these events occur during the first 90 s of the simulation, and a few more occur at later times, until the amplitude of the propagating wave becomes too small to get over the bump.

Figure 4 shows a comparison of the model simulated SSH with the measured values at the seven SSH measurement locations shown in Fig. 2. The simulated SSH is a bit higher than observed at gauges 3–5 and 7, but the overall agreement of the SSH is fairly good and the timing of the SSH peaks in the model simulation is also fairly good.

3.4 Dam Break Flow around a 90° Corner

This test case involves the simulation of a WAD laboratory experiment that was conducted by the group of Professor Y. Zech at the Universite Catholique de Louvain, Belgium (Soares Frazao and Alcrudo 1999). This experiment has been used for verification of WAD models by other researchers including Soares Frazao et al. (1999), Viseu et al. (1999), and Guan et al. (2013), and a later, slightly modified version of this experiment was used by Soares Frazao and Zech (2002) and Biscarini et al. (2007). The setup for this experiment is shown in Fig. 5. A tank of water of horizontal size 2.39 by 2.44 m is filled to a depth of 0.53 m with water. The tank is connected by a gate to a channel of width 0.495 m. At a distance of about 4 m from the tank, the channel makes a right-angle turn to the left. Note that the floor of the channel is 0.33 m above the bottom of the tank and is 0.20 m below the initial level of the water within the tank. When the gate of the tank is opened, the water flows from the tank down the channel and around the 90° corner of the channel. The water height within the tank and at five locations along the channel was measured by gauges. The locations of these six gauges are shown in Fig. 5. Note that the five gauges within the channel are located in the center of the channel.

NCOM was set up for this test case with a horizontal grid resolution of 0.02 m. Beyond the back end of the experimental setup shown in Fig. 5, a catch basin of 1-m width, 0.8-m depth, and running the full length of the back of the numerical grid was used to collect the water flowing out of the end of the channel. The third-order upwind scheme was used for momentum advection. Quadratic bottom drag was used with a bottom roughness of 6×10^{-5} m and a minimum value of the bottom drag coefficient of 0.0001 (see Section 2.5). This bottom roughness gives a bottom drag coefficient similar to the Manning bottom drag used by Guan et al. (2013), who used a Manning coefficient of 0.013 s/m$^{1/3}$. Both the NCOM and Manning bottom drag formulations give a bottom drag coefficient of about 0.0038 for a water depth of 0.08 m and a bottom drag coefficient of about
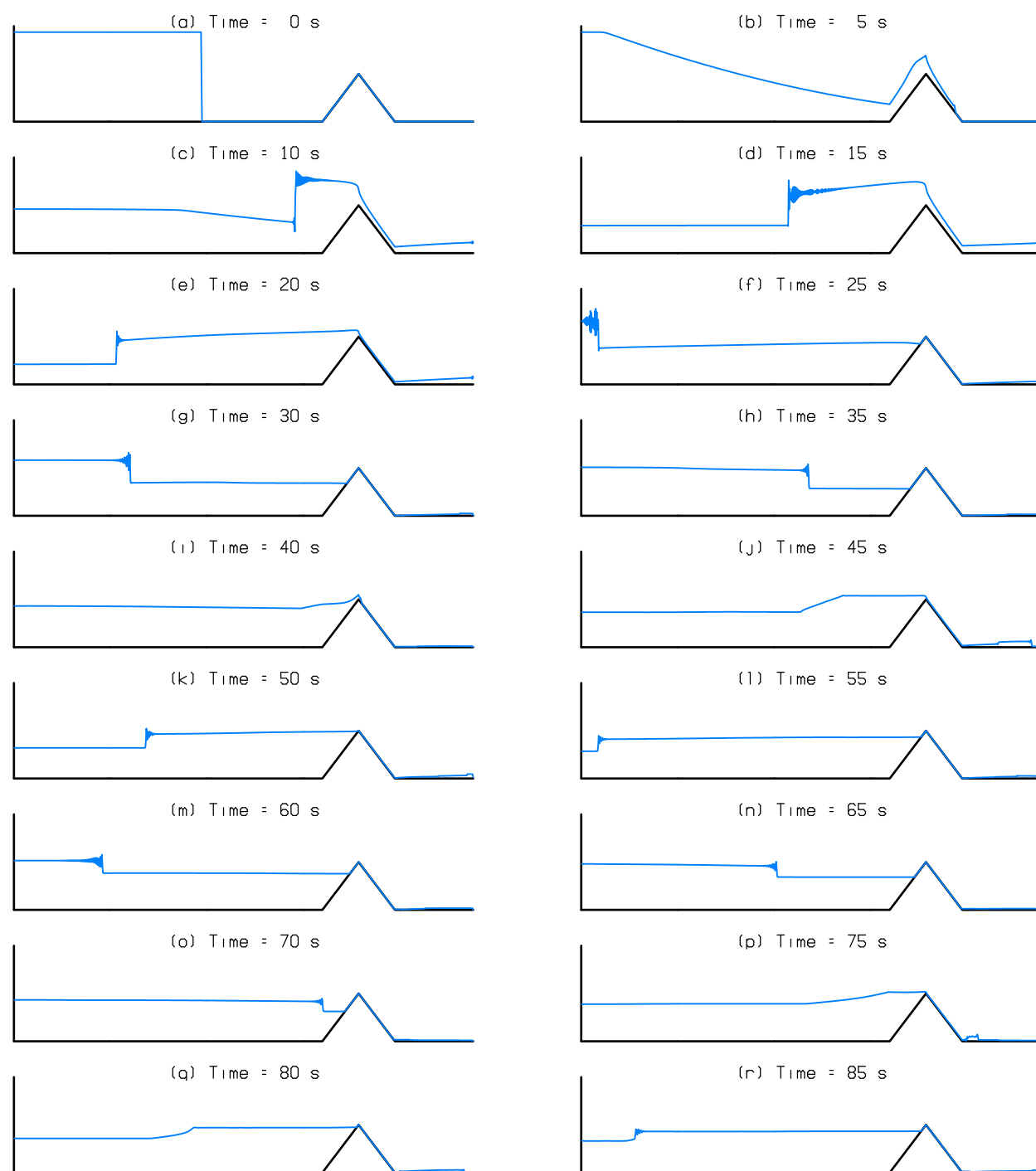
Fig. 3 — SSH from model simulation of dam-break flow over a triangular bump at 5-s intervals.
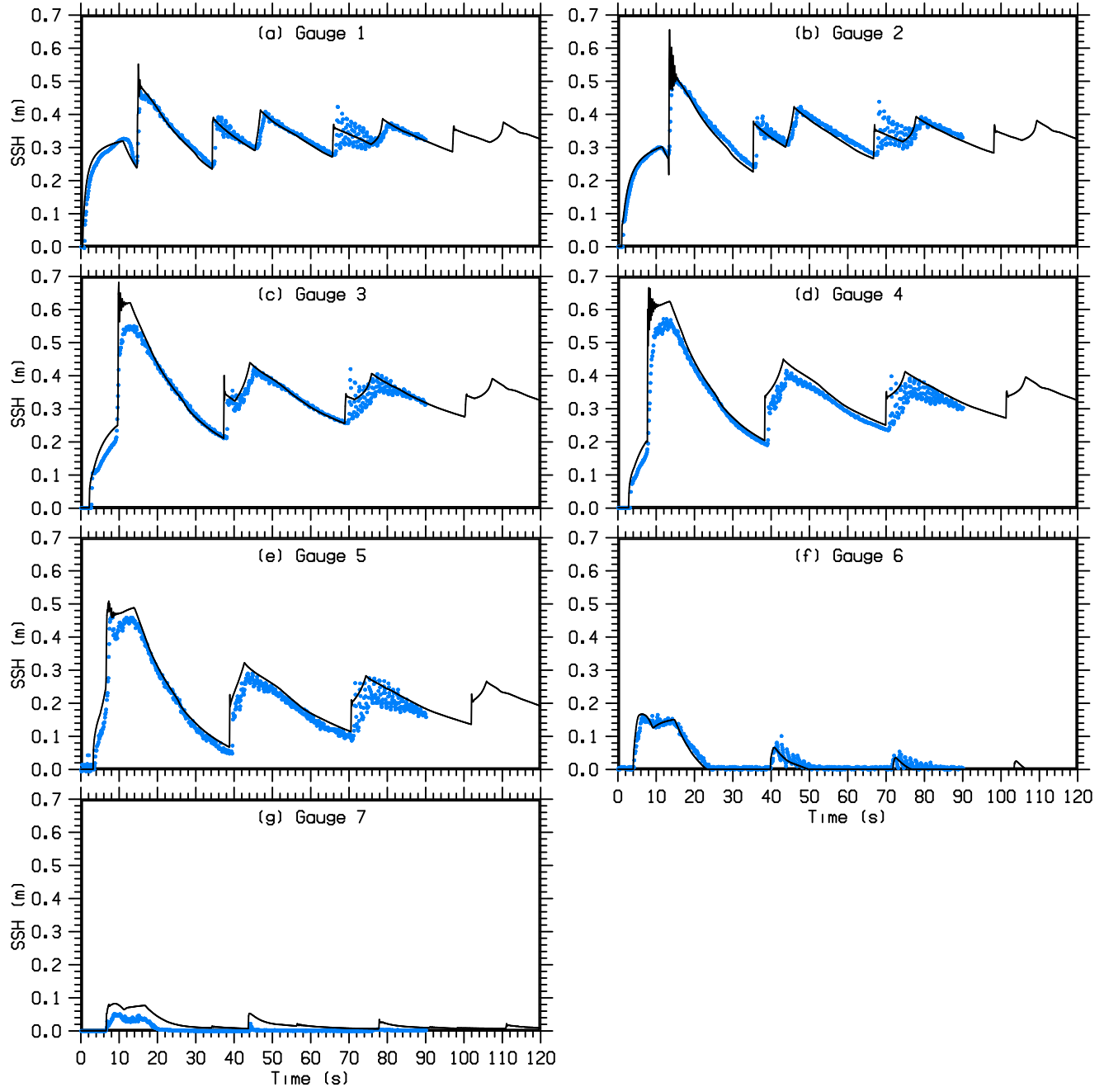
Fig. 4 — Comparison of observed (blue dots) and model-simulated (black line) SSH at the 7 measurement locations shown in Fig. 2 for the dam-break flow over a triangular bump.
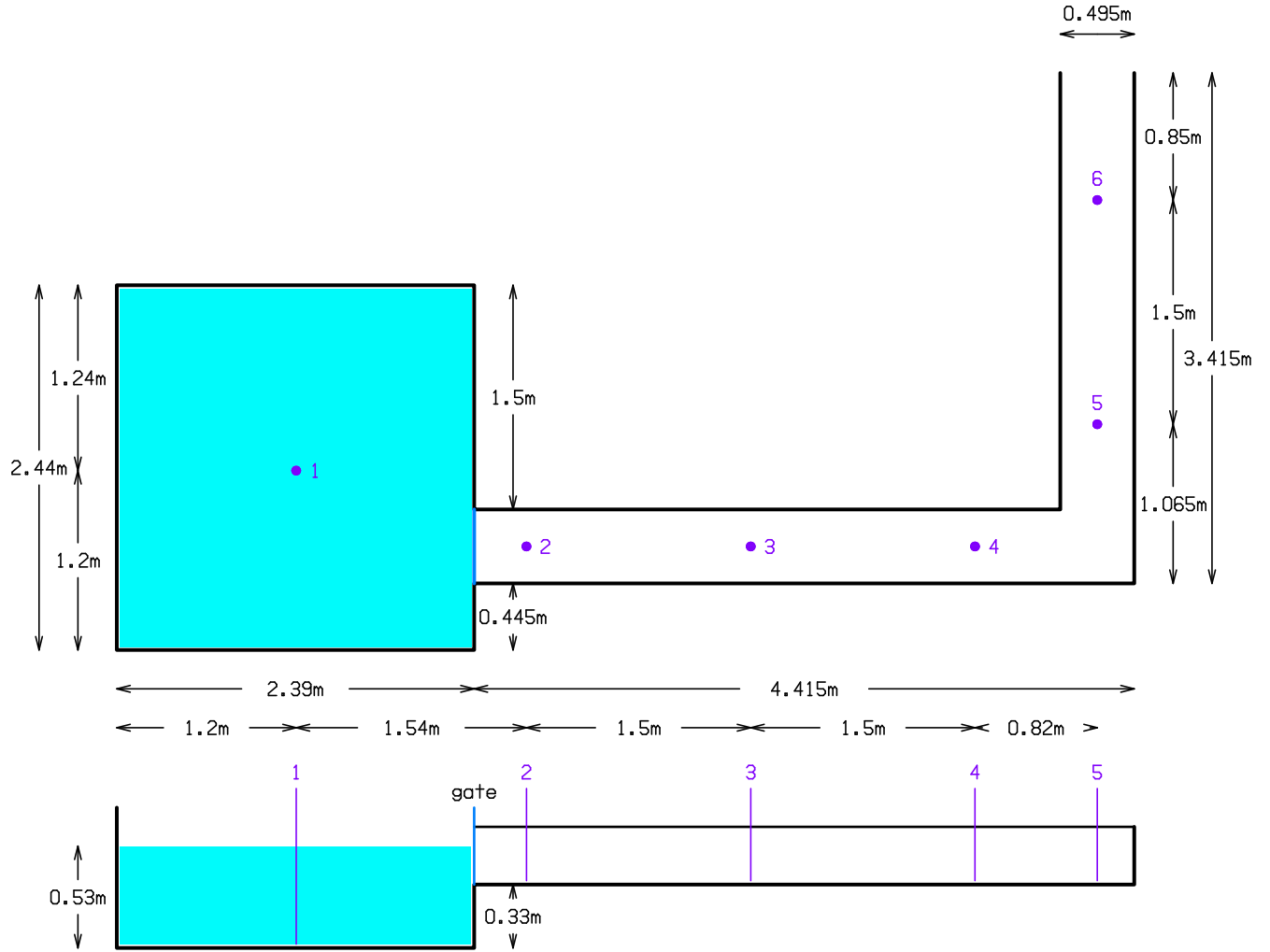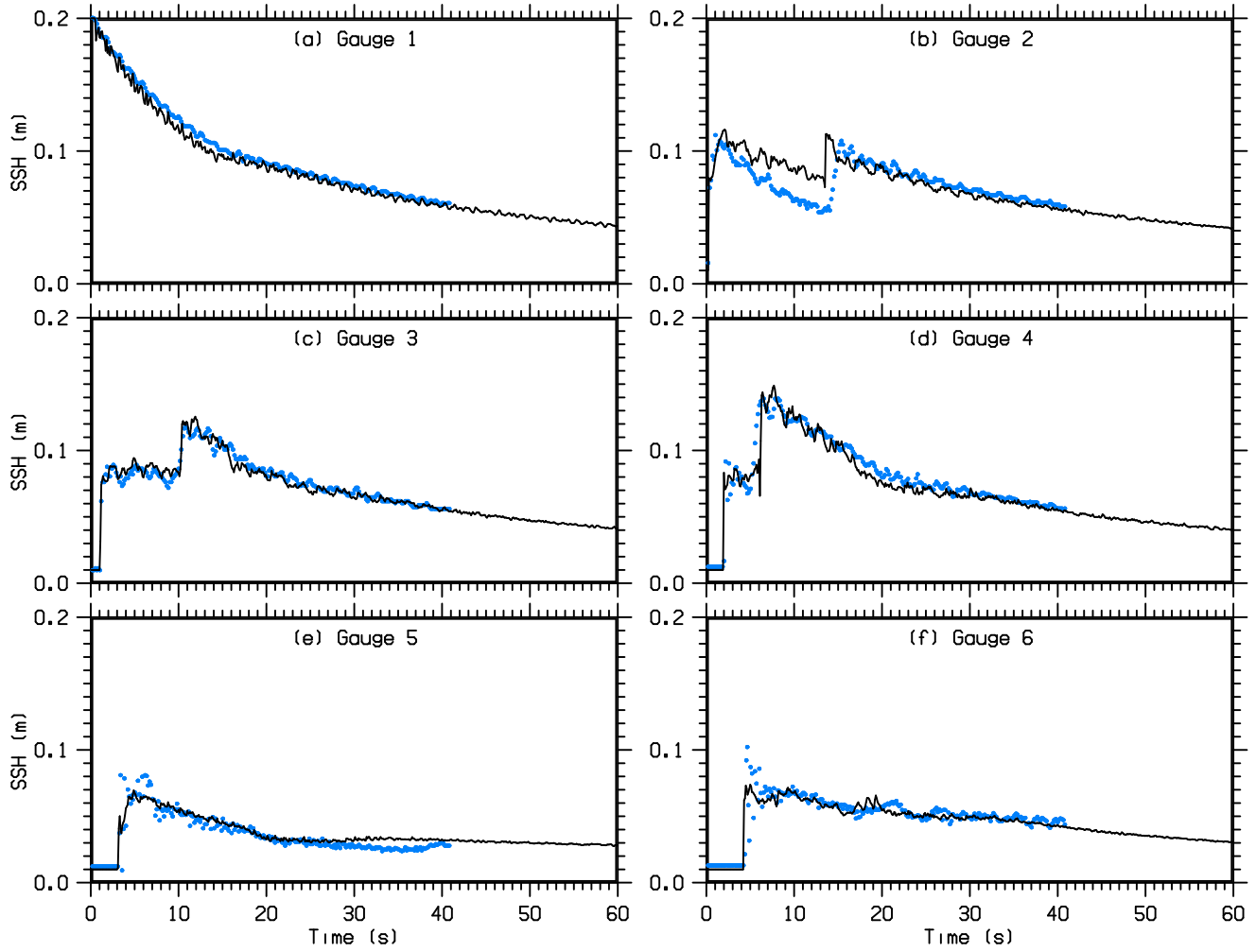
Fig. 5 — Setup and dimensions for laboratory experiment for a dam-break flow into a channel and around a 90°
corner. Top and side views are shown. The gate between the tank and the channel is drawn in dark blue. The six
SSH measurement locations are shown in purple.

Fig. 6 — Comparison of observed (blue dots) and model-simulated (black line) SSH at the 6 measurement locations shown in Fig. 5 for the dam-break flow around a 90° corner.

0.0045 for a water depth of 0.05 m. The minimum water depth D_{min} for the WAD was set to 0.01 m. The time step used was 0.002 s. The simulation was run for 60 s and output from the simulation was saved at 0.1-s intervals.

Figure 6 shows a comparison of the model simulated SSH with the measured values at the six SSH measurement locations. The measured values correspond to the laboratory experiment that was run with a "wet" bed, with an initial water depth of 0.01 m within the channel. The results at gauges 3–6 in Fig. 6 are fairly similar to those obtained by Guan et al. (2013) (the latter did not show results for gauges 1 and 2).

The SSH at gauge 1 shows the simulated drop of the water level within the tank to be in good agreement with the observed drop. The SSH at gauges 2–4 within the first section of the channel shows the time of arrival of the wetting front at each of these locations, and also a later jump in the SSH due to the arrival of an upstream propagating wave caused by reflection of the original wetting front at the end of the first section of the channel. The time of arrival of the reflected wave at gauges 4, 3, and 2 in the first section of the channel is about 6, 11, and 15 s, respectively.

The worst agreement between the simulated and measured SSH in Fig. 6 is at gauge 2 up until the arrival of the reflected wave at about 15 s; after that the simulated SSH agrees well with the measured value. A similar discrepancy between the simulated and measured SSH at gauge 2 was noted by Soares Frazao and Alcrudo (1999), and can be seen in Soares Frazao and Zech (1999) in their Fig. 6b. The SSH at gauges 5 and 6 in the second section of the channel shows the arrival of the original wetting front and the gradual drop of the SSH as the water drains away.

The model results were found to be fairly sensitive to the bottom drag, which was noted by Soares Frazao and Alcrudo (1999). With a lower bottom drag, the flow of water down the channel increases in speed, the water level within the tank drops more quickly, the upstream propagation of the wave reflected at the end of the first section of the channel is slowed because of the increased speed of the flow in the channel, and the water drains out of the second section of the channel more quickly. The latter effect is especially noticeable in lower water levels at gauge 6 after the arrival of the wetting front. All of these changes from the use of a lower bottom drag tend to reduce the agreement with the measured SSH relative to the results in Fig. 6.

3.5 San Francisco Bay

Most of San Francisco Bay (SFB) is relatively shallow, and the bay has a variety of areas that are subject to WAD. For these reasons and the fact that we had done some earlier work in SFB during which we had realized that a WAD capability was needed to conduct proper simulations in this area, SFB was used as the primary, realistic, test case for testing during the development of NCOM's WAD scheme. Simulations of SFB were run at resolutions of 500, 200, and 100 m and in single-layer barotropic mode and in multi-layer baroclinic mode. The coarser resolution runs allowed for quicker turn-around, while the higher resolution runs provided better resolution of the finer-scale features of the bay and broader, more extensive, WAD areas in terms of the number of grid points involved.

Note that there are a number of low-lying areas around SFB that are not regularly flooded at high tide because they are protected by dikes. Many of these areas were once part of the bay, e.g., marshlands, but have since been reclaimed for various uses. Since the dikes are often fairly narrow, they usually aren't well resolved in bathymetric data bases for SFB. Hence, if one computes a bathymetry for SFB from such data bases, the WAD areas may appear to be more extensive than they actually are. One can examine some of the low-lying areas derived from the bathymetric data bases using, for example, Google Maps, and see there is human activity occurring in many of these areas, e.g., farms, buildings, etc., that would not be there if the areas were regularly flooded. However, for the purpose of testing the ability of an ocean model to perform WAD in a variety of situations, whether an area does actually flood at high tide may not be all that relevant, i.e., having more extensive WAD areas tends to provide a better test of the robustness of the WAD ability of the model, except, of course, if comparing the model results with observations in or near these areas.

Figure 7 shows the domain and bathymetry used for most of the SFB simulations. The depths are with respect to mean sea level (MSL). The two plots in Fig. 7 show the depths contoured between zero and -100 m, and between -8 and +2m, the latter to better illustrate the bathymetry in the shallow areas of the bay. The maximum tidal amplitudes in SFB are about 1 m. Grid cells with an elevation greater than +2 m are defined to be land areas that are outside the computational domain and these areas are shown in black.
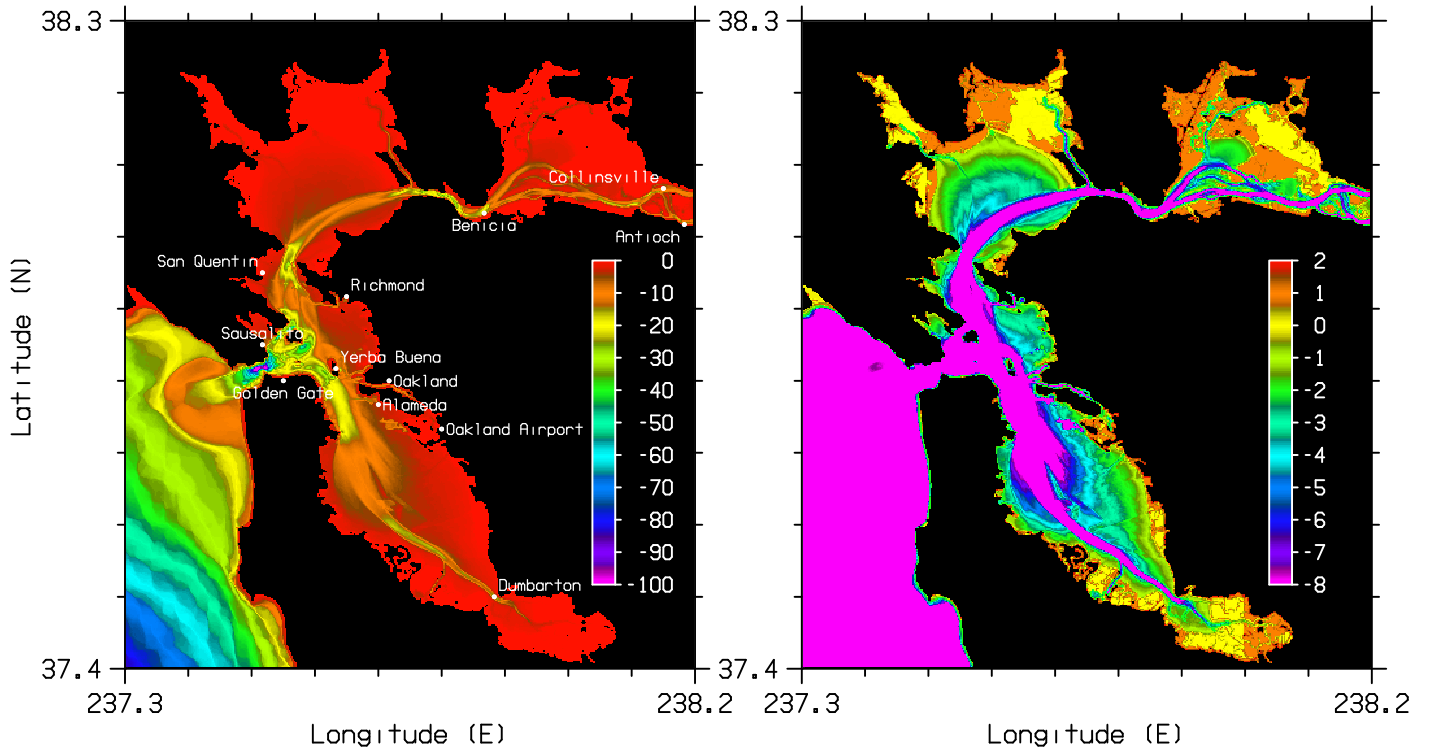
Fig. 7 — Domain and bathymetry used for SFB simulations. The plot on the left shows the depths contoured between zero and -100 m depth. The locations of IHO stations are labeled. The plot on the right shows the depths contoured between -8 and +2 m to better illustrate the bathymetry in the shallow areas.

SFB is composed of three main areas: the northwestern part is San Pablo Bay, the northeastern part is Suisun Bay, and the southern part is sometimes referred to as South Bay. The San Pablo and Suisun Bays are connected by the Carquinez Strait. The greatest depths within SFB are about -100 m in the mouth of the bay, where there is extensive bottom scouring due to the strong tidal currents. Most of the rest of SFB outside the main channels is fairly shallow, i.e., less than 5 m deep. As noted previously, some of the low-lying areas are protected from flooding by dikes. However, some of these protected areas are not accounted for in Fig. 7, since the dikes are not very well resolved in the bathymetric data base that was used, and having more extensive WAD areas was considered to be useful for the purpose of testing the WAD. Another issue with the bathymetric data base used for Fig. 7 is that the precision of the land elevations is only to the nearest meter. This can be seen in Fig. 7b by the lack of shading of the color contours in the areas that have an elevation above 0 m.

To generate fluctuating water levels within SFB, tidal forcing was applied at the open boundaries, which lie outside SFB, for the eight main tidal constituents: K_1, O_1, P_1, Q_1, K_2, M_2, N_2, and S_2. This tidal forcing (i.e., the tidal SSH and current transports) was obtained from one of the tidal data bases (i.e., the $1/12°$ West Coast data base) developed at Oregon State University (OSU) by Egbert and Erofeeva (2003). Tidal potential forcing within the interior of the domain was found to have little effect on the tides in the simulations because of the relatively small size of the domain.

During the testing of NCOM's WAD scheme, over 140 simulations in SFB were conducted

looking at different bathymetries, different horizontal grid resolution (500, 200, and 100 m), different vertical grid resolution (single and multiple layers), different types of vertical grids (hybrid sigma/z-level and generalized vertical coordinate), different physics (barotropic and baroclinic), different input parameters, different values of the minimum allowed water depth D_{min} for WAD (10, 5, 2, 1, and 0.1 cm), different numbers of computer processors, and different numerical precision (single and double precision). All the simulations ran smoothly as long as (i) the time step was sufficiently small to prevent instability due to exceeding the advective CFL limits, and (ii) the errors we found, which were related to the changes being made for the WAD, were corrected (many of these simulations were conducted during the development of the WAD scheme).

Figure 8 shows a comparison of the model-simulated tide with the observed tide at the International Hydrographic Office (IHO) stations within SFB shown in Fig. 7. The model-simulated tides are for a 40-layer, fully baroclinic simulation on the 200-m SFB grid. The comparison is fairly good except at Oakland Airport, which in the model simulation is in an area of severely restricted circulation due to the presence of some islands and very shallow depths (Fig. 7). If the location of the model point used to represent the Oakland Airport IHO station is moved southwest out of the area of restricted flow, the model-simulated tide agrees well with the observed tide. It is likely that the bathymetry near this IHO station is not adequately resolved and/or is too shallow.

Also, the model-simulated tide at the three IHO stations in Suisun Bay in the northeastern part of SFB do not agree with the observed tide as well as at most of the other stations. This may, in part, be due to the fact that the model domain (a) over-represents the WAD areas, and (b) has a closed boundary on the eastern end of Suisun Bay and does not include the extension of the delta areas of the Sacramento and San Joaquin Rivers further to the east.

The total area of the SFB domain in Fig. 7 that is within the computational domain, i.e., not including the black-colored areas in Fig. 7, is about 2820 km^2. For the tidal simulations, the area that always remains wet is about 2160 km^2, the area that always remains dry is about 270 km^2, and the area of WAD, i.e., the area that is sometimes wet and sometimes dry, is about 390 km^2. These areas represent 76%, 10%, and 14% of the computational domain, respectively.

Figure 9 shows sea-surface temperature (SST) and sea-surface salinity (SSS) within SFB from a 500-m-resolution, multi-layer, baroclinic simulation with variable temperature and salinity. The temperature and salinity were initialized from the climatological annual mean values. The forcing for this simulation is from the tides and river inflows. The river inflows are the annual mean for the Sacramento and San Joaquin Rivers, which are about 682 and 213 m^3/s, respectively. These are, by far, the two largest rivers flowing into SFB and both flow into the eastern end of Suisun Bay. The bathymetry used for this simulation is different from that in Fig. 7 in that the areas cut off from tidal flooding by dikes are mostly accounted for; hence, the horizontal extent of the WAD areas is significantly reduced.

The SST in Fig. 9 is at 10 d into the simulation and shows the cooling of the water in the mouth of SFB due to vertical mixing by the strong tidal currents, which at this time are ebbing. The SSS in Fig. 9 is at 100 d, which is when the salinity distribution within the bay in this simulation has almost reached equilibrium. The salinity in Suisun Bay in Fig. 9 is fairly low due to the large river inflows.

A summary of some of the results from the simulations in SFB with respect to the WAD are
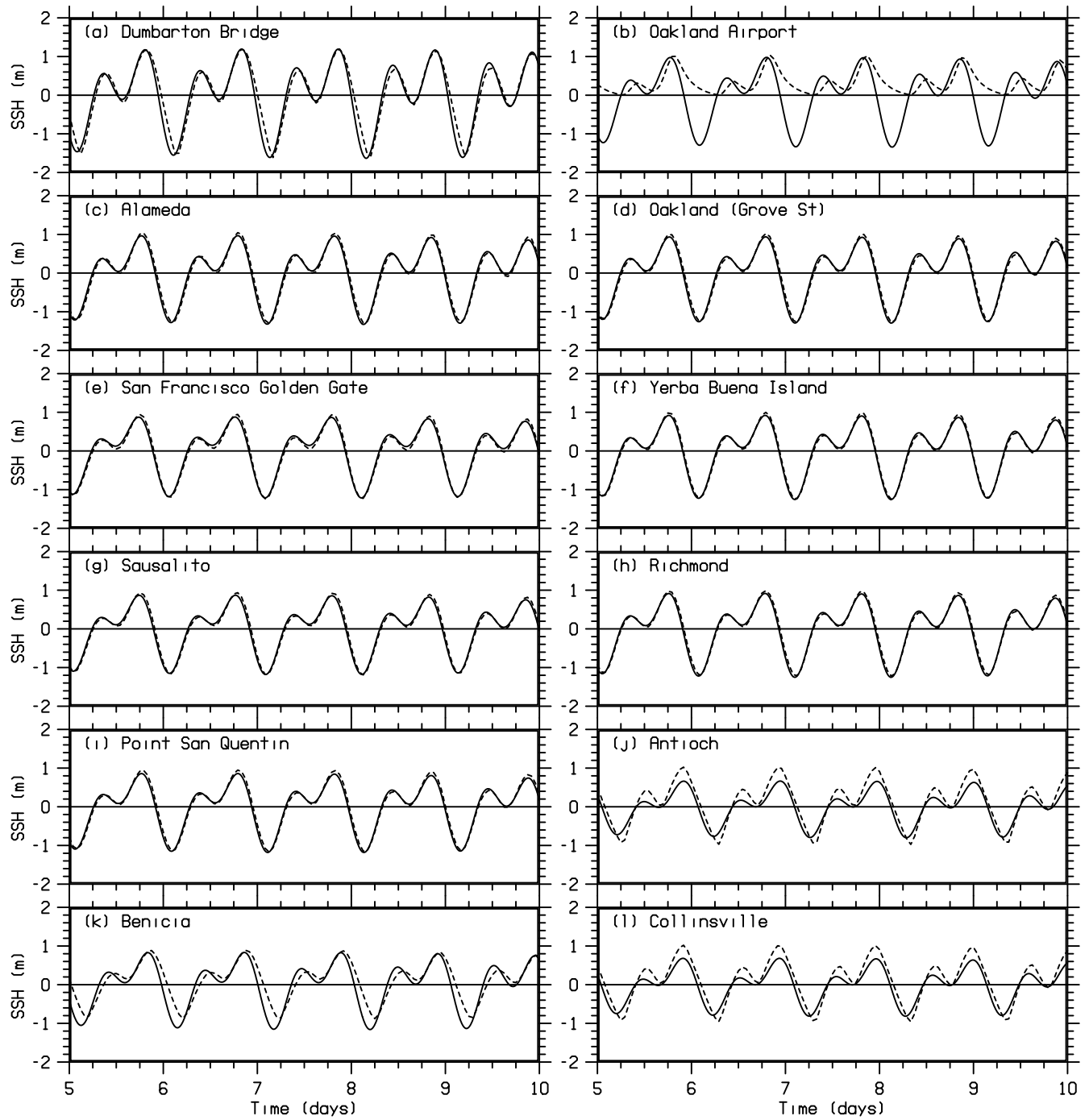
Fig. 8 — Comparison of observed (solid line) and model-simulated (dashed line) tide at the location of several IHO tidal stations within SFB. The time period of the plots is January 6–10, 2004.
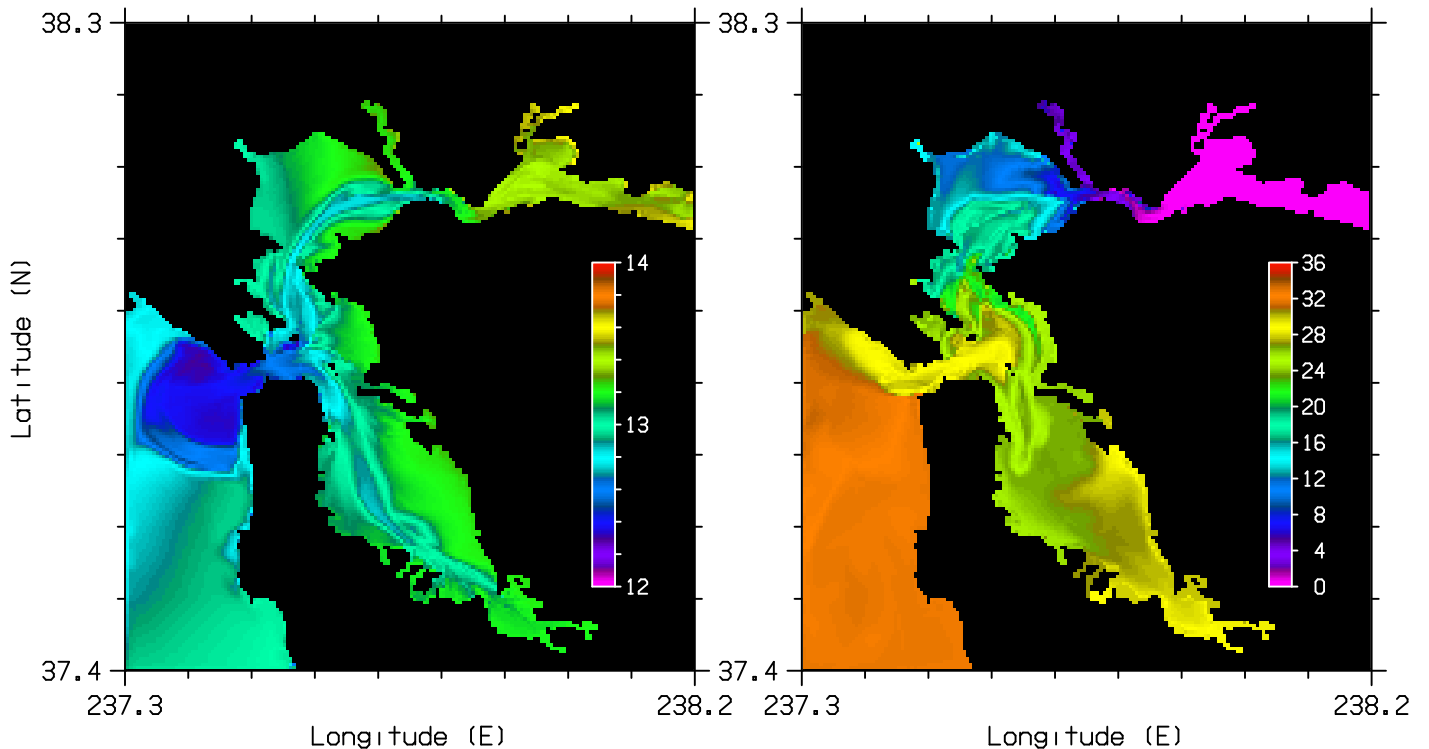
Fig. 9 — SST in °C at 10 d (left) and SSS in psu at 100 d (right) for a multi-layer, baroclinic simulation of SFB with river inflows.

as follows. Simulations tend to run more smoothly with larger time steps when the bathymetry is smoother due to lower values of the maximum advective CFL values. Baroclinic simulations with multiple layers tend to require smaller time steps as the number of layers is increased due to the decreasing thickness of the layers and the increased possibility of exceeding the CFL limit for vertical advection. Double precision (i.e., more than 32-bit precision for real numbers) is needed for accurate conservation of scalar fields on our workstations, especially for long simulations without data assimilation, and for high-resolution simulations with a small time step (since the cumulative effects of roundoff error tend to increase with the number of time steps). Both the advection and vertical mixing terms tend to be a source of roundoff error, i.e., fixing just one or the other does not solve the roundoff error problem. If a scalar field (e.g., salinity) is initialized to a constant value, and the values transported in or out through the boundaries and through source or sink terms in the interior are the same, constant value, then the constant value of the scalar field will be maintained to good accuracy if double precision is used (this is a useful test for tracer conservation). The use of the Flux-Corrected-Transport (FCT) scheme for the advection of scalar fields is effective for preventing advective overshoots. The sigma/z-level (SIGZ) and generalized vertical coordinate (GVC) versions of the NCOM code give almost identical results for the same model setup (note that identical results are not possible due to unavoidable differences in the sequence of some of the calculations).

3.6 Chesapeake Bay

Chesapeake Bay (ChB) is referred to as a "partially mixed" estuary. Relatively high salinity water from the ocean flows into and northward, up the bay, near the bottom, and fresher water

from a number of rivers flows into the bay and southward, down the bay, near the surface and out of the mouth of the bay. This type of circulation within a bay is referred to as an "estuarine" circulation.

Due to mixing between the inflowing, higher salinity water near the bottom and the fresher water near the surface, there is a gradual decrease in the salinity of the near-bottom, saltier water as it flows up the bay and a gradual increase in the salinity of the fresher water as it flows southward near the surface towards the mouth of the bay. In spite of this vertical mixing, at most locations within ChB, there is a significant vertical salinity stratification (Stroup and Lynn 1963); hence, the estuary is referred to as being "partially mixed".

The annual mean freshwater inflow from the rivers into ChB is about 2000 m^3/s and the mean of the inflowing seawater into the bay is on the order of 7000 m^3/s (Valle-Levinson et al. 1998), so that the mean of the outflow from the bay is on the order of 9000 m^3/s. Simulations of the estuarine circulation in ChB with NCOM by Martin (1999) developed estuarine flow volumes and a salinity structure within ChB similar to the observed values. Note that the salinity structure in this simulation took over a year to reach a fairly steady state (Martin 1999).

Recently, numerical model simulations were conducted by the Naval Research Laboratory (NRL) Code 7320 in the Chesapeake Bay area in support of the Trident Warrior 2013 (TW13) Naval Exercise (Allard et al. 2014). Since the tidal amplitude in this area tends to be less than 1 m, it was decided to set the shallowest bottom depth H at sea points to -2 m for the simulations to avoid drying out grid cells during the ocean model runs. This limit worked satisfactorily during the exercise itself, which took place during the summer when the winds tend to be light. However, during spin up of the ocean model domain, which was begun in January 2013, strong winds during the winter caused drying out of some areas within ChB and along the coast due to set down of the SSH in excess of 2 m.

Since a beta-test version of NCOM with WAD was available at this time, it was decided to use the new WAD capability of NCOM for the spin up to avoid having to deepen the shallowest allowed bottom depth beyond the -2 m that had originally been used to set up the ocean model domains for TW13. Hence, NCOM with WAD was used to spin up the ocean circulation, and this spinup was then used to initialize some of the TW13 ocean forecasts. The spinup was run from the beginning of January to the end of June 2013. Note that, as mentioned above, this is too short a time to allow full development of the salinity structure within ChB; hence, the salinity structure within and just outside ChB for this spinup was initialized from a 2-year spinup from earlier work with NCOM in ChB. This was blended with salinity values in the deeper water from Global HYCOM, which also provided the initial conditions for the SSH, ocean current, and temperature fields.

Forcing for the spinup consisted of the following: monthly climatological river inflows for the seven largest rivers flowing into ChB (the James, York, Rappahannock, Potomac, Patauxent, Patapsco, and Susquehanna) with a combined annual mean inflow of 2220 m^3/s and the Delaware River in Delaware Bay with an annual mean inflow of 570 m^3/s, tidal forcing at the open boundaries for the eight main tidal constituents (K_1, O_1, P_1, Q_1, K_2, M_2, N_2, S_2) from the OSU 1/12° Atlantic Ocean tidal database and tidal potential forcing over the interior for the same eight constituents, 3-hourly values of atmospheric forcing from the operational COAMPS West Atlantic model (consisting of surface atmospheric pressure, wind stress, and solar and net longwave radiation, and latent and sensible surface heat fluxes computed using the COAMPS winds and air temperature

and humidity and the NCOM SST, which provides some feedback to the surface heat fluxes from the NCOM SST), and daily boundary conditions for the SSH, current velocity, temperature, and salinity fields from Global HYCOM.

Figure 10 shows the domain used for the spin up. The grid is 115×226 points and the horizontal resolution is 2 km. The relatively coarse grid is the reason these plots look a bit blocky. The vertical grid uses a total of 40 layers, with 19 sigma layers between the surface and the bottom down to a maximum depth of -105 m, and with 21 fixed-depth levels (z-levels) between -105 m and -2800 m. The vertical grid was smoothly stretched downward from the surface, with an upper-layer thickness of 0.95% of the total depth of the sigma part of the grid; hence, the thickness of the upper layer is about 1 m in water deeper than -105 m and is proportionally less in water shallower than -105m. Note that the depths in Fig. 10a are only contoured between zero and -100 m to provide more detail in the bays and on the shelf. The depths in this domain increase substantially past the edge of the continental shelf. The maximum depths within this domain are about -2800 m near the southeast corner.

Figure 10b shows water depths within the computational domain contoured within the range of -4 to -2 m to illustrate areas of potential WAD. Without WAD, set down of the SSH and drying out of grid cells in some of these shallow areas caused the model to crash. With WAD, the model spinup ran smoothly through the entire January-June period without a problem each of the several times it was run (several different spinups were conducted with different bathymetries).

Figure 11 shows the SST and SSS at the end of the spinup of the ChB domain on 30 June 2013. The SST shows some cooling along the coast due to the moderately strong south winds that were occurring at this time. The SSS shows the large variations of salinity in ChB and Delaware Bay. The SSS at the head of these bays is fairly low and increases towards the mouth of the bays due to mixing with saltier water traveling up the bays near the bottom. The south winds and upwelling along the coast have reduced the SSS signature of the outflow plume from ChB outside the mouth of the bay.

We refer to the setup used here for ChB as an example of "occasional" WAD, i.e., the focus was not on simulating the WAD of extensive areas, but of maintaining robust performance of the ocean model during the occasional times when relatively shallow grid cells dry out. The purpose of including this simulation of ChB in the VTR was to illustrate the use of such occasional WAD to maintain numerical stability in a relatively long (6-month) NCOM simulation. Since the WAD procedure was only invoked occasionally, there was fairly negligible additional computer time required for the WAD calculations that were needed.

3.7 Cook Inlet, Alaska

Cook Inlet (CI) is located on Alaska's south-central coast. The upper part of CI has a tidal range of over 10 m, and these are the second highest tides in North America after the Bay of Fundy in Nova Scotia. In part due to the large tides, CI has extensive WAD areas, which are composed mostly of tidal mud flats that are exposed during low tide. CI has been used for testing both tidal prediction and WAD in numerical models by other investigators, e.g., Matthews and Mungall (1972), Oey et al. (2007), and Kowalik and Proshutinsky (2010).

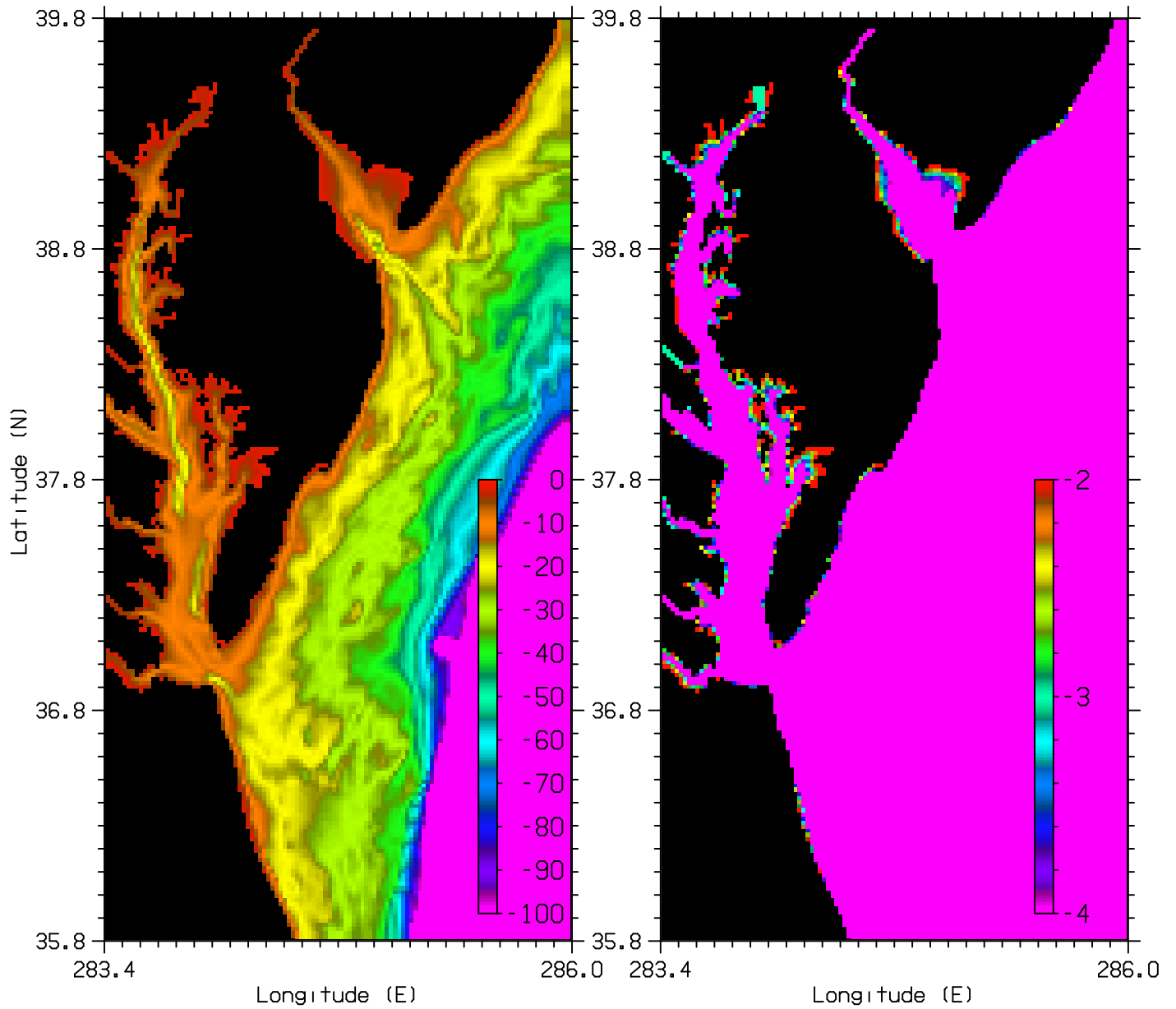Figure 12 shows the domain and the bathymetry used for the numerical simulations of the tides

Fig. 10 — Domain and bathymetry used for Chesapeake Bay simulations. The plot on the left shows the depths contoured between zero and -100 m depth. The plot on the right shows the depths contoured just between -2 and -4 m to indicate areas where WAD can potentially occur.
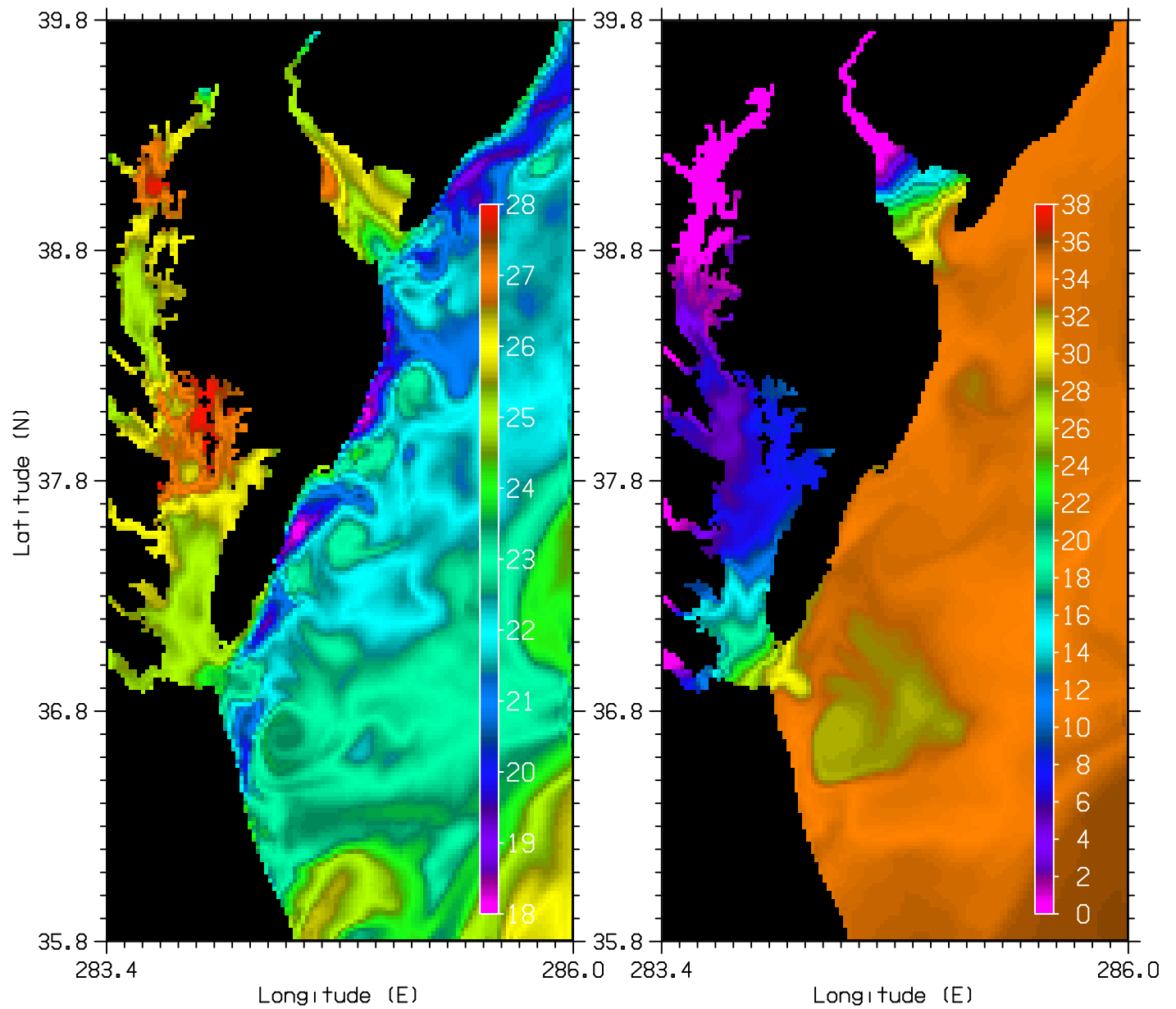
Fig. 11 — SST (left) in °C and SSS (right) in psu at the end of the spinup of the ChB domain on 30 June 2013

in CI. The town of Anchorage, Alaska is located in the northeastern part of CI where the waters of CI separate into Knik Arm to the northeast and Turnagain Arm (TA) to the east-southeast. Note that the eastern two thirds of TA is relatively shallow and at low tide consists mostly of exposed tidal mudflats. As the rising tide enters the eastern two thirds of TA, a tidal bore is usually generated by the rapidly rising tide, which propagates eastward up TA. The island just west of Anchorage is called Fire Island, and at low tide it is possible to walk from Anchorage to Fire Island on the exposed mud flats, though the rapid advance of the flooding tide and the quicksand-like properties of occasional soft areas on the mudflats can be treacherous both here and in most of the other WAD areas in CI.

The bathymetry for CI in Fig. 12 was, for the most part, obtained from the National Oceanic and Atmospheric Administration (NOAA) Digital Environmental Model (DEM) Number 937, which has a resolution of 24 s (about 1 km) and is one of a number of such data bases being developed by NOAA for tsunami and flood prediction and is available online. However, this and other bathymetry data bases we investigated for CI had poor accuracy in many areas, notably in the WAD areas and in the NE part of CI including Knik Arm and TA. This is and has been a significant problem for those trying to model the tides and WAD in CI.

However, we were able to obtain some more accurate, high- (50–100 m) resolution, bathymetry data for the NE part of CI from Tal Ezer (personal communication) and these data are included in Fig. 12. Tal Ezer and Hua Liu have been working on developing a bathymetry for this area using a combination of satellite photographs and tidal data to determine the location of the land-sea boundary at various phases of the tide and thereby deduce the bathymetry (Ezer and Liu 2009, 2010). The bathymetry data developed by Ezer and Liu (EL) includes depths in the WAD areas estimated from the satellite and tidal data and in the deeper areas from nautical charts.

The horizontal grid resolution used for the tidal simulations in CI was about 1 km and the horizontal dimensions of the longitude-latitude grid were 312×356 points. Only a single layer was used in the vertical. A quadratic form of the bottom drag was used (see Section 2.5) with a minimum value for the bottom drag coefficient of 0.0025 and a bottom roughness of 0.01 m. The third-order upwind scheme was used for momentum advection. Tidal forcing was from the OSU $1/12°$ Pacific Ocean data base. The eight main tidal constituents (K_1, O_1, P_1, Q_1, K_2, M_2, N_2, and S_2) were used for the tidal forcing. The time step used was 30 s.

Figure 13 shows a comparison of the predicted tide with the tide computed at eight IHO tidal stations within and just outside CI (the locations of these IHO stations are noted in Fig. 12). The observed tide was computed using the IHO data for the same eight tidal constituents that were used for the model simulation. The time period in Fig. 13 is the beginning of day 6 through day 10 of the model simulation (i.e., January 6 through 10, 2001). (All the times referred to here are GMT.) Note that this time period includes a sampling of the highest tides regularly observed in CI. The close agreement at the Seward tidal station in Fig. 13d, which is outside CI on the south facing coast east of the mouth of CI (Fig. 12), suggests that the accuracy provided by the OSU Pacific tidal database that was used to provide the tidal boundary conditions is very good.

The overall agreement of the observed and simulated tides in Fig. 13 is quite good. There is a slight lag in the predicted tidal phase and a slight overprediction of the tidal amplitude at the Fire Island and Anchorage tidal stations in the NE part of CI. Both of these errors could probably
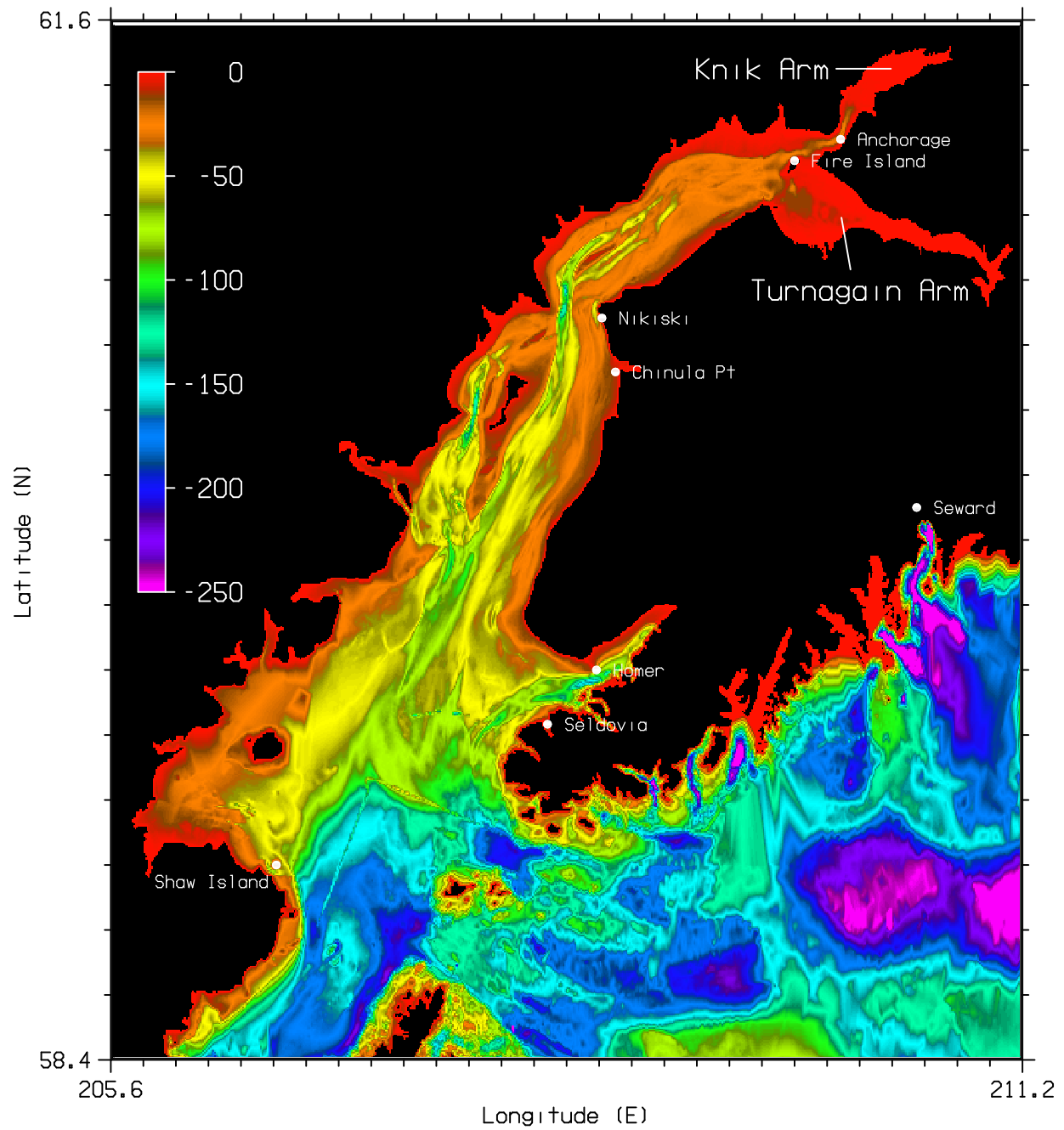
Fig. 12 — Bathymetry for Cook Inlet. Depths are relative to mean sea level. Areas with land elevations greater than 8 m are outside the computational domain and are shown in black. The locations of eight IHO stations are labeled.
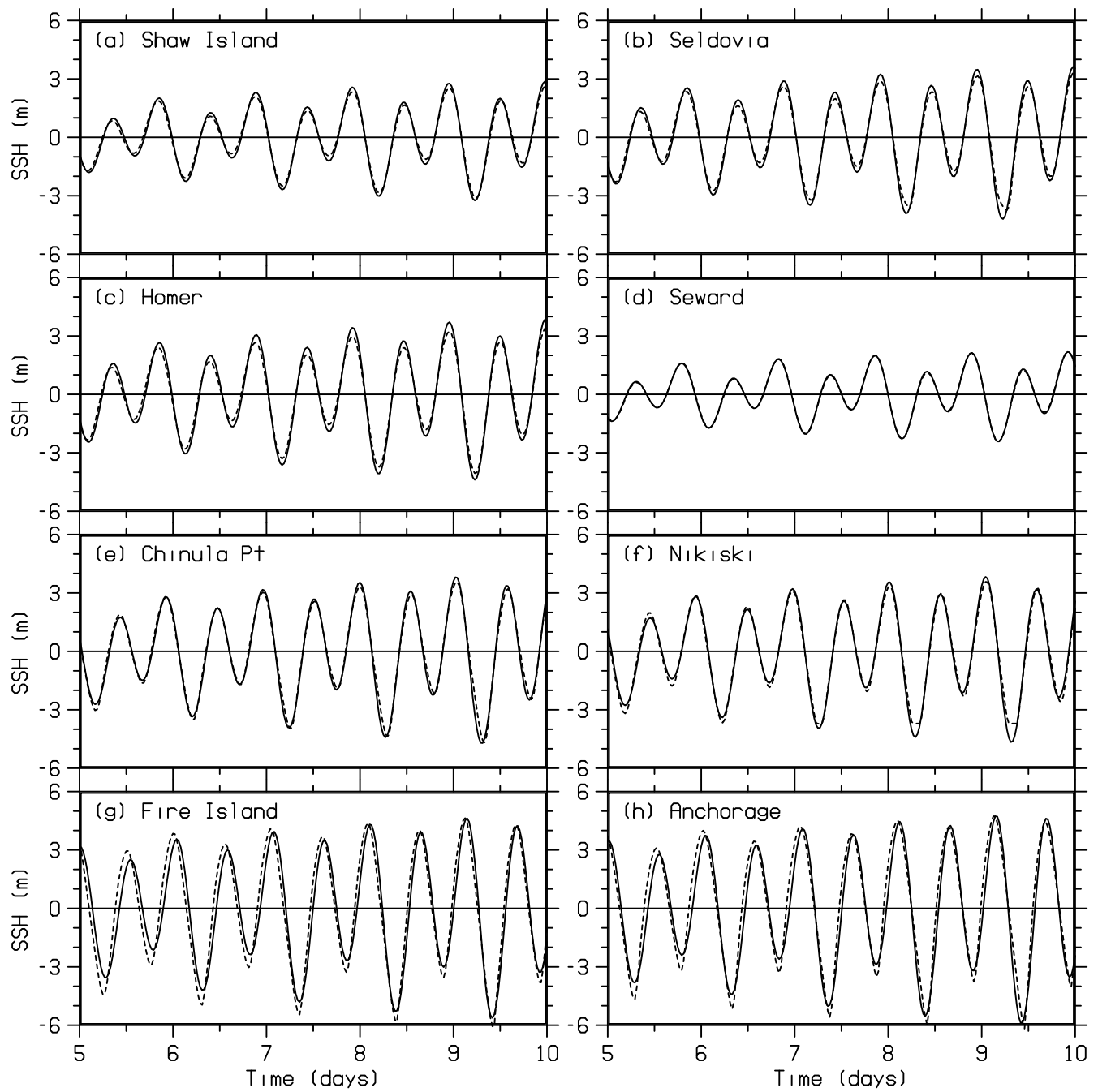
Fig. 13 — Comparison of observed (solid line) and model-simulated (dashed line) tide at several IHO stations within Cook Inlet. The time period of the simulations is January 6 through 10, 2001.

be reduced by increasing the damping of the tide as it propagates up CI by slightly increasing the bottom drag.

There are many WAD areas within Cook Inlet and along the coast just outside of Cook Inlet. As noted earlier, the bathymetry in these areas is, with respect to the accuracy needed for validating a WAD model, not very well known. However, within the narrow, upper two-thirds of Turnagain Arm (TA) in northeast CI, the bottom is almost fully exposed at low tide and there is a tidal bore that propagates up TA on the flooding tide. The tidal bore is a popular attraction in this part of Alaska, and can easily be observed from the Seward Highway that runs along the north side of TA. The approximate times of occurrence of the bore at several locations along TA are provided to assist those wishing to view the bore. Because of the availability of this information on the tidal flooding that occurs in TA, it was decided to focus the validation of WAD in CI on the WAD that occurs in TA.

Figure 14 shows the bathymetry in the northeast part of CI, which includes both Knik Arm and TA, provided by Tal Ezer. The bathymetry is contoured between -5 and +5 m to highlight the WAD areas. Figure 14 shows the locations of the Fire Island and Anchorage IHO stations and the names of several landmarks along the northern side of TA.

The time of passage of the tidal bore as it propagates up TA is available at the locations along TA labeled in Fig. 14 relative to the time of low tide at Anchorage. These observed times are listed in Table 1. For the model simulations, the times of arrival of the tidal bore listed in Table 1 are taken to be the time at which the SSH exceeds the minimum SSH during the previous low tide at that location by 0.5 m. Note that the values in Table 1 for the model simulations are an average over nine low tides between January 6 and 10, 2001.

Table 1 — Comparison of observed and model-predicted tidal bore arrival times in Turnagain Arm with respect to time of low tide at Anchorage. Values are in minutes and are an average over nine low tides between January 5 and 10, 2001.

Expt	Beluga Pt	Indian Pt	Bird Pt	Girdwood	Portage
obs	75	90	135	180	300
1	286	338			
2	175	208	303	343	431
3	179	210	307	348	446
4	113	136	213	260	343
5	53	79	153	201	338
6	57	83	158	203	316
7	56	84	162	208	320

Calculation of the arrival times for the tidal bore for our initial tidal simulation for CI found the simulated bore to lag far behind the observed bore (see Expt. 1 in Table 1). For this simulation, the tidal bore did not propagate very far beyond Indian Pt. and so no arrival times are given for locations beyond Indian Pt. for Expt. 1 in Table 1.

In order to try to increase both the speed and extent of the tidal flooding in TA, the bottom drag was significantly reduced, i.e, the minimum value of the bottom drag coefficient $C_{b_{min}}$ was
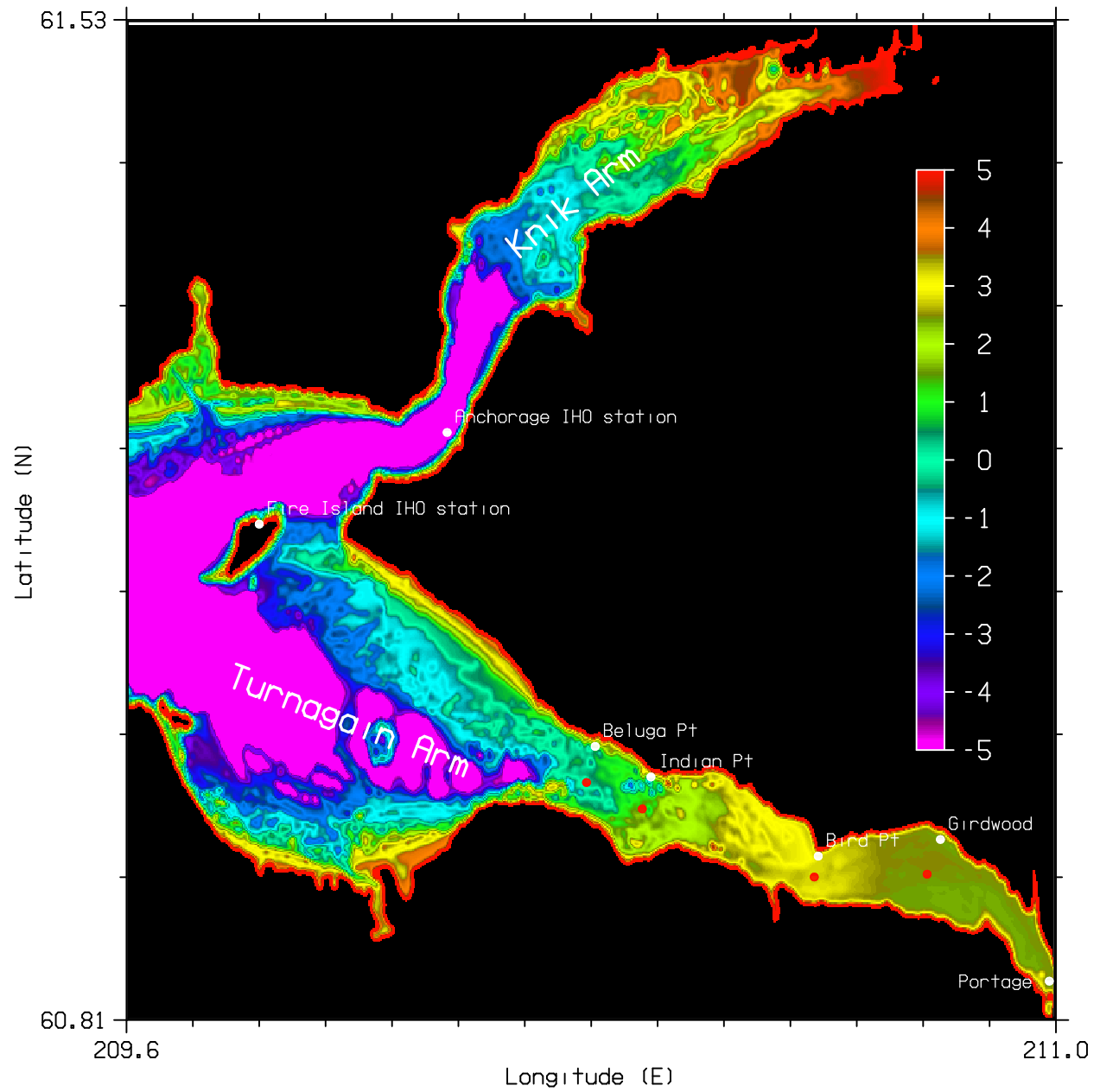
Fig. 14 — Bathymetry for the northeast part of Cook Inlet provided by Tal Ezer. Depths are with respect to MSL. The locations of the Fire Island and Anchorage IHO stations are indicated and the locations of several landmarks along the northern side of Turnagain Arm are also shown.

reduced from 0.0025 to 0.0001 and, just within the shallow areas of TA, the bottom roughness was reduced from 0.01 to the very small value of 10^{-20} m so as to maintain $C_b = C_{b_{min}}$ in the WAD areas (see Section 2.5). This reduction of the bottom drag significantly increased the extent of the tidal flooding in TA, but still resulted in very large lags in the model-simulated bore times relative to the observed times (see Expt. 2 in Table 1).

One possible factor contributing to the slow arrival of the tidal bore in TA relative to the time of low tide at Anchorage is the presence of some shallow features in the western third of TA, including a shallow ridge connecting the mud flats on the north and south sides of TA, which can be seen in Fig. 14. This shallow ridge blocks the tidal drainage out of the part of TA east of the ridge, and also delays the arrival of the tidal flood east of the ridge. Hence, the bathymetry in the wider, western third of TA was modified by imposing an approximately 4-km wide channel though the middle of the western third of TA, with a maximum depth of -12 m near the mouth of TA and a maximum depth of -4 m near the beginning of the narrow, eastern two thirds of TA. These changes in the bathymetry allowed for improved drainage of the tide and a quicker arrival of the flood just east of the (now removed) ridge. However, the arrival time of the bore at locations along the narrow, upper two thirds of TA was not improved (see Expt. 3 in Table 1). This delay now appeared to be due mainly to the large increase in the bottom elevation at the beginning of the narrow part of TA near Beluga Pt., which rises from -4 m to 0 m over a distance of a few km.

At this point, it was decided to try more extensive modification of the bathymetry in the narrow, eastern two-thirds of TA. The minimum depth in TA near Beluga Pt. in Fig. 14 is about 0 m and the minimum depth rises to about +2 m near Indian Pt. The minimum depth of 0 m near Beluga Pt. would seem to make it difficult for the tidal flood to arrive at this location much before the tide in the western part of TA rises to this level, which would be about 3 hrs after the occurrence of low tide. This analysis is consistent with the arrival times of the bore at Beluga Pt. for Expts. 2 and 3 in Table 1. Another problem is that the depth in the narrow part of TA in Fig. 14 reaches a maximum of about +3 m at Bird Pt. and then decreases towards the end of TA near Portage. This raises the question of how the area above Bird Pt. is to drain if the bottom slopes the wrong way.

The simplest idealized bathymetry to try was considered to be a linear variation of the bottom slope along the entire, narrow, eastern two-thirds of TA. Hence, a linear bottom slope was tried with a minimum depth of -4 m at the beginning of the narrow part of TA just west of Beluga Pt. and a minimum depth of +3 m at the end of TA near Portage. This gives minimum depths at Beluga, Indian, and Bird Pts. and at Girdwood of -3.4, -2.9, -0.3, and +1.3 m, respectively. Experiment 4 in Table 1 shows the predicted bore times in TA for this simulation. The results with respect to the earlier experiments are noticeably improved, but the simulated bore still significantly lags the observed bore, i.e., the lags at Beluga, Indian, and Bird Pts. and at Gridwood are 38, 46, 78, and 43 minutes, respectively. Note that the steady increase in the minimum elevation along the upper two-thirds of TA in this simulation does allow most of the water in this part of TA to drain out at low tide.

At this point in our investigation of the tidal bore in TA, Tal Ezer notified us that a new bathymetry for CI was available from NOAA (Zimmermann and Prescott 2014) and suggested we look at it. We contacted Mark Zimmermann of NOAA's Alaska Fisheries Science Center in Seattle, who helped us obtain this bathymetry. The Zimmermann and Prescott (ZP) bathymetry is at 50-m resolution and covers almost all of the interior of CI, except for a small area near the mouth of

CI. The ZP bathymetry was interpolated to our model grid, and the NOAA DEM 937 bathymetry was used for the areas in our domain not covered by the ZP bathymetry. The ZP bathymetry as received was referenced to mean lower low water (MLLW). To convert the vertical datum to MSL, we used our tidal solution for CI along with the difference between MSL and MLLW at several tidal stations within CI provided online by NOAA (Table 2). Note that the correction is about 5 m in the NE part of CI.

Table 2 — Difference between MSL and MLLW (m) at
several IHO tidal stations in CI.

Homer	Seldovia	Nikiski	Anchorage
1.69	2.90	3.44	5.02

Figure 15 shows the ZP bathymetry in the NE part of CI for the same region shown in Fig. 14 for the bathymetry from Tal Ezer. Comparison of Fig. 15 with Fig. 14 shows significant differences. For the ZP bathymetry, the flow through the western third of TA is less obstructed by shallow areas, and the minimum bottom elevation in the eastern two-thirds of TA up to Girdwood is significantly lower. Both of these differences should help to advance the arrival time of the tidal bore in TA.

With this revised bathymetry for CI, the predicted tidal amplitudes at Fire Island and Anchorage were about 0.8 m lower than observed for the highest tides. Hence, the bottom roughness in the main part of Cook Inlet was reduced from 0.01 to 0.003 m, which resulted in increased tidal amplitudes in the NE part of CI that agreed better with the observed tides. This change in the bottom roughness in the main part of CI was used for all the simulations conducted with the ZP bathymetry.

Experiment 5 in Table 1 shows the predicted bore times for a tidal simulation with the ZP bathymetry. The time of the bore with respect to low tide at Anchorage is significantly reduced relative to the previous experiments, except at Portage where the elevation (4 m) is now higher than in the previous simulations. However, the presence of some isolated deeper pockets in the eastern two thirds of TA (Fig. 15) prevent these areas from draining completely during the tidal ebb. The water depth at low tide in some of these pockets exceeds 5 m.

Figure 16 shows plots of SSH versus time for Expt. 5 for Anchorage and for the locations along TA. The locations along TA never completely dry out for any length of time, except at Portage. The SSH at Beluga, Indian, and Bird Pts. shows a bit of noise at low tide, which is due to some residual drainage occurring in these areas between the remaining pockets of water. Because of the incomplete drainage in Expt. 5, some simulations were conducted with the ZP bathymetry with modified depths in the eastern two-thirds of TA to try to achieve more complete drainage.

Experiment 6 in Table 1 shows the predicted bore times for a tidal simulation with the ZP bathymetry with the minimum depth at Beluga Pt. set to -5.5 m and minimum depths at Indian and Bird Pts. and at Girdwood and Portage of -4.55, -1.5, +0.5, and +5.1 m, respectively. These minimum depths yield a bottom slope along the thalweg of TA between Beluga Pt. and Girdwood of about 2 m per 10 km. The bore times are generally slightly improved over Expt. 5.

Figure 17 shows plots of SSH versus time at Anchorage and along TA for Expt. 6. An extensive dry period occurs during low tide at Bird Pt., Girdwood, and Portage, as indicated by the flattening of the SSH during low tide at these locations. At Beluga and Indian Pts., a brief dry period occurs
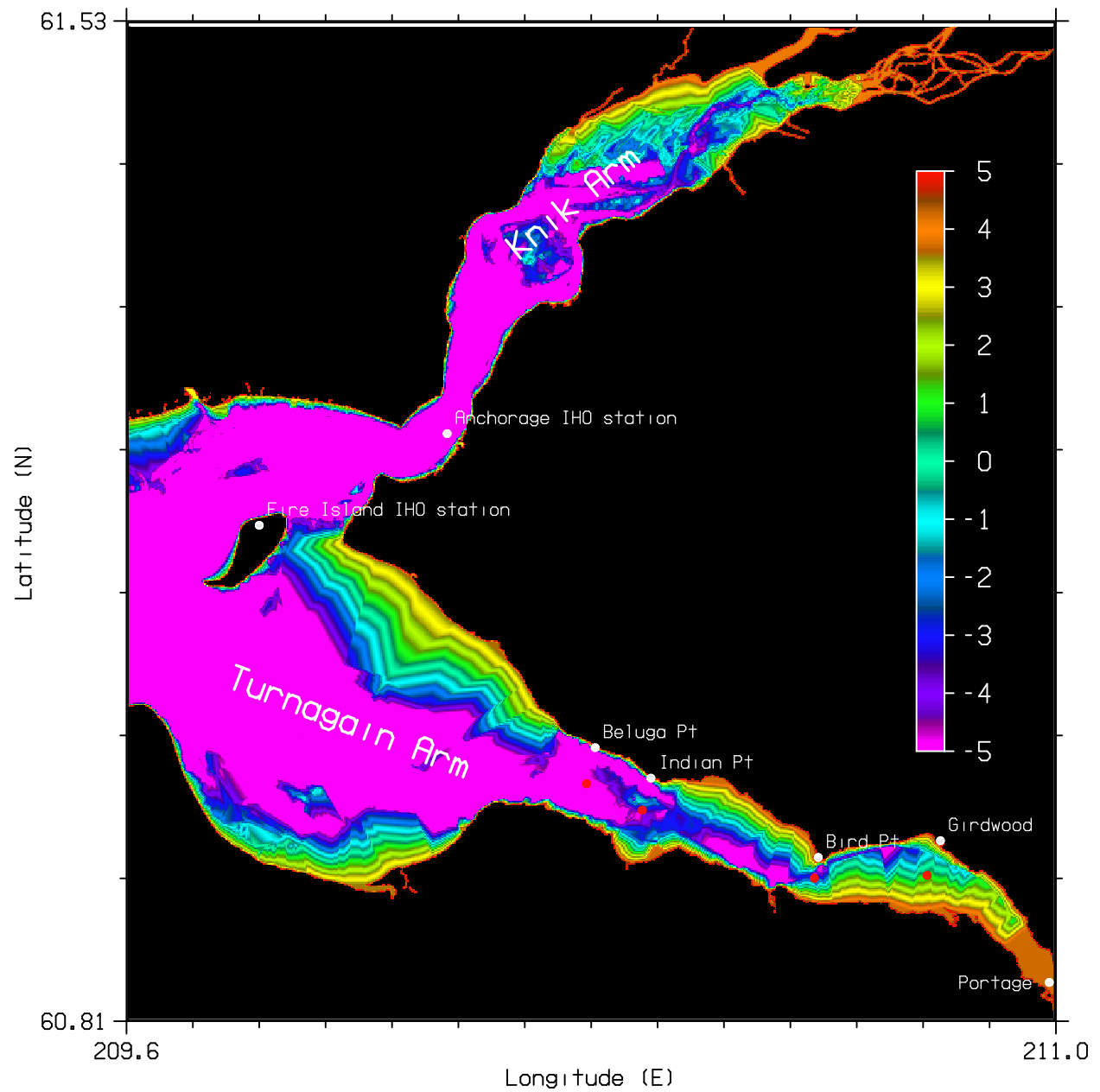
Fig. 15 — Depths in the northeast part of CI from the CI bathymetry of Zimmermann and Prescott (2014). Depth are relative to MSL. The locations of the Fire Island and Anchorage IHO stations are indicated and the locations of several landmarks along the north side of Turnagain Arm are also shown.
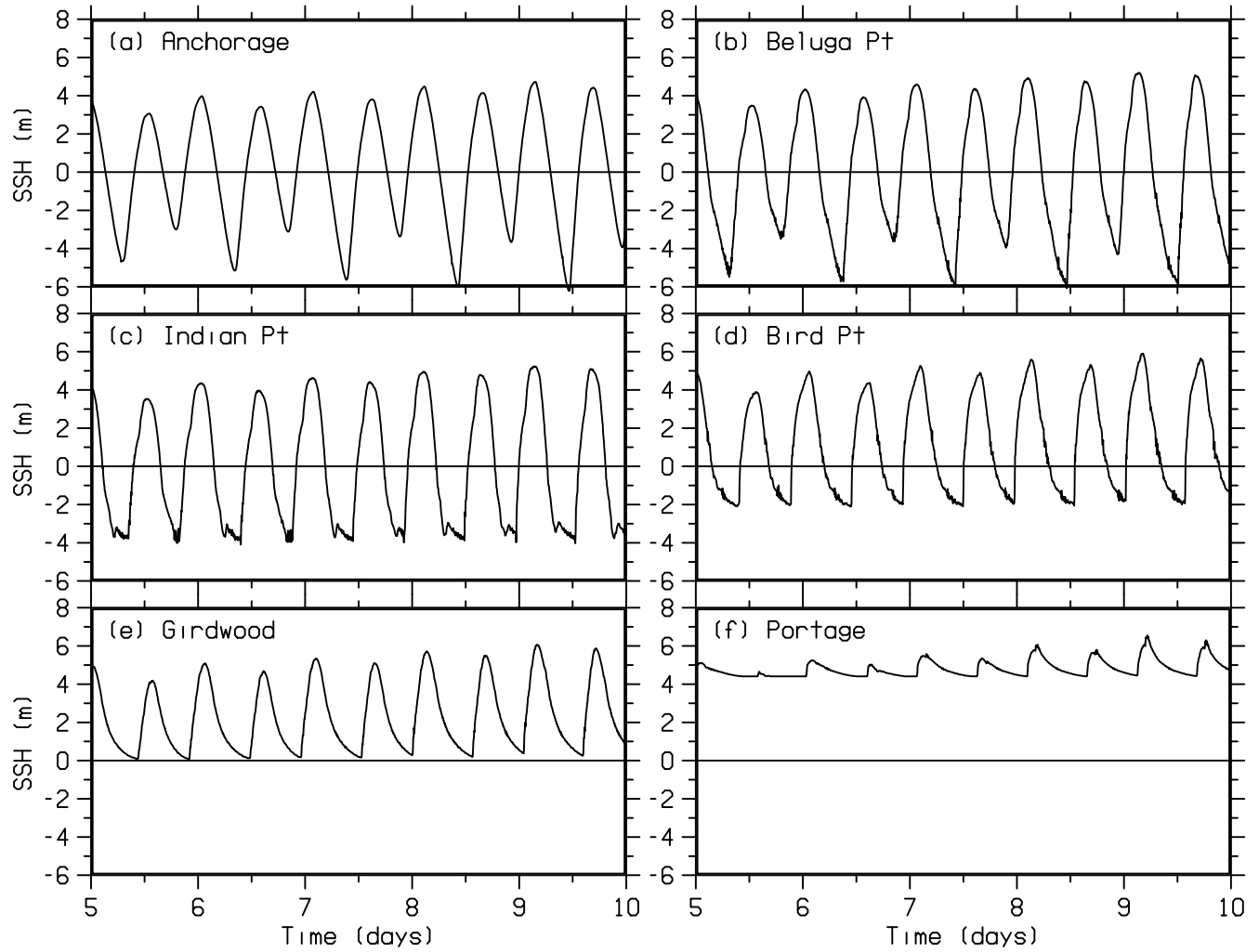
Fig. 16 — Plots of SSH vs time for Expt. 5 at the Anchorage IHO station and at several locations along TA from January 6 through January 10, 2001.
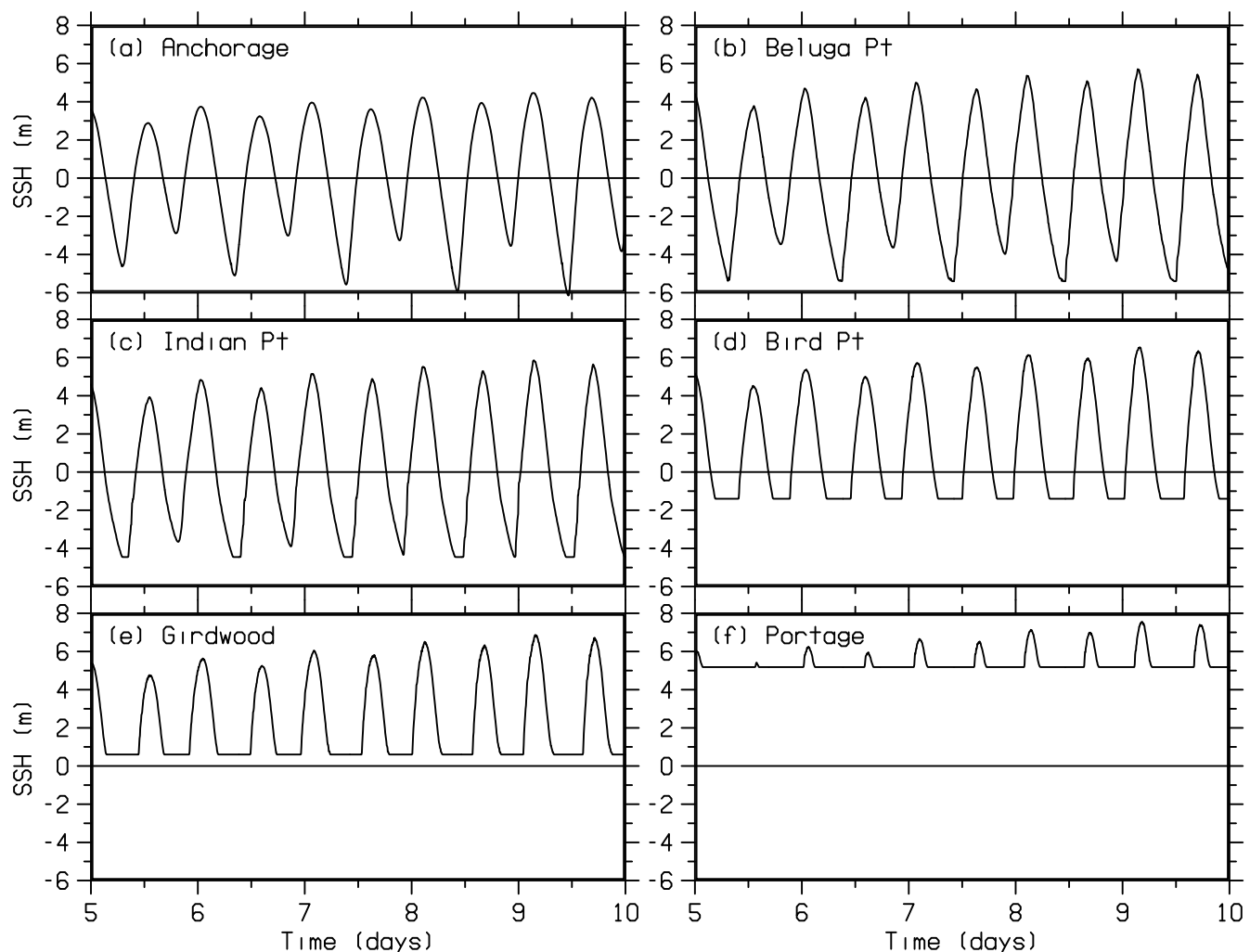
Fig. 17 — Plots of SSH vs time for Expt. 6 at the Anchorage IHO station and at several locations along TA from January 6 through January 10, 2001.

on the lowest tides. The lack of noise in the SSH at low tide compared with Fig. 16 indicates that there is not much residual drainage occurring at low tide. The increase in the maximum SSH along TA in Fig. 17 indicates the effect of momentum conservation (inertia) on the tidal flood in TA. This effect is partly dependent on the narrowing of TA from west to east. The increase in the SSH along TA also depends on the bottom drag and would be reduced if the bottom drag were increased.

Experiment 7 in Table 1 shows the predicted bore times for a tidal simulation with the ZP bathymetry with the minimum depths between Beluga Pt. and Girdwood increased by 0.5 m over the corresponding depths used for Expt. 6, and the minimum bottom depth at Portage increased by 0.2 m to 5.3 m. This change was made to see if the drainage at Beluga Pt. could be improved over Expt. 6. These minimum bottom depths increase the elevation of the bottom between Beluga Pt. and Girdwood by 0.5 m, but maintain the same bottom slope in this area. (It was found that lower bottom slopes in this area tend to reduce the degree of drainage at Beluga Pt.) Table 1 shows the bore times are slightly increased by this change, which was expected. Plots of the SSH versus time along TA (not shown) look similar to the results for Expt. 6 in Fig. 17, though the period of drying at Beluga Pt. is slightly increased over Expt. 6.

The total area of the CI domain in Fig. 12 that is within the computational domain, i.e., not including the black-colored areas, is about 37200 km^2. For the Expt. 7 tidal simulation, the area that always remains wet is about 32350 km^2, the area that always remains dry is about 1970 km^2, and the area of WAD, is about 2880 km^2. These areas represent 87%, 5%, and 8% of the computational domain, respectively.

Looking at just the area within CI itself, the total area that is within the computational domain is about 21020 km^2. For Expt. 7, the area that always remains wet is about 17180 km^2, the area that always remains dry is about 1300 km^2, and the area of WAD is about 2540 km^2, which represent 82%, 6%, and 12% of the computational domain within CI, respectively.

The WAD in the eastern two thirds of TA depends on a number of factors. These include the bathymetry in the western third of TA and, in the eastern two thirds of TA, the bottom depths and slope, the channel width and cross-sectional shape, and the bottom drag. There is a significant amount of uncertainty in all these aspects of TA. In addition, the existence of small drainage channels (Ralston and Stacey 2007) and the porosity of the bottom in TA are not accounted for in our simulations and probably affect the drainage to some extent. Because of these uncertainties, trying to guess the proper parameters for TA is a process that could go on indefinitely. Hence, we did not try further refinements of the simulation of the tidal bore in TA for this report.

The simulations of the tidal bore in TA that were conducted here do suggest a few points. The western third of TA must be sufficiently deep and clear of obstructions that the tidal flow entering the eastern two thirds of TA is not too restricted and is of sufficient volume. The bathymetry provided to us by Tal Ezer seems to be too shallow and restricted in the western third of TA. Part of the problem may be that the depths are referenced to something lower than MSL, and need to be deepened. The ZP bathymetry as received was referenced to MLLW. In adjusting this bathymetry to MSL, the depths in the entire northeastern part of CI were deepened significantly, i.e., by about 5 m. The use of this bathymetry resulted in a strong, rapid response of the tidal flood at the entrance to the narrow, eastern two thirds of TA with respect to the time of low tide at Anchorage.

Similarly, the bottom depth near Beluga Pt. cannot be too shallow. This would seem to be indicated by the fairly rapid appearance of the tidal bore observed at Beluga Pt. after the time of low tide at Anchorage (75 minutes). If the bottom elevation near Beluga Pt. is too high, the tidal flood there will be delayed until the SSH in the western part of TA rises sufficiently to allow the tide to enter the narrow, eastern two thirds of TA. The effect of inertia and conservation of momentum can push the tidal height near Beluga Pt to elevations higher than those in the western part of TA; however, the simulations we conducted suggest that this effect is insufficient to match the observed time of the tidal bore if the bottom elevation at Beluga Pt. is much higher than about -3 m.

If the tide in the eastern two thirds of TA is to drain, then there must be a fairly constant upward slope from west to east, so that the water can drain. Observations seem to indicate that though some water may remain behind, most of the water in the eastern two thirds of TA drains out at low tide. We also found that, for most of the water to drain out of the eastern part of TA at low tide, the bottom slope must be sufficiently steep. To get some time period of complete drainage at Beluga Pt. on the lowest tides in the simulations we conducted required a bottom slope of about 2 m per 10 km.

3.8 Hurricane Ike

Hurricanes are associated with large storm surges and coastal flooding. These processes are important to capture when using a WAD model. In this section, the WAD caused by Hurricane Ike along the Texas and Louisiana coasts in September 2008 is simulated and the results are compared with observations.

Ike made landfall on September 13, 2008 near Galveston, TX as a category 2 hurricane (Veeramony et al. 2014). Ike caused significant flooding and the water levels during the storm were observed at a number of locations. Hence, Hurricane Ike provides a useful test case for the verification of a WAD model.

The domain and bathymetry used for the simulations of Hurricane Ike are shown in Fig. 18a. Figure 18b shows the bathymetry and land elevations along part of the Texas and Louisiana coasts up to a height of 10 m. The bathymetry in Fig. 18 is the same as that used by Veeramony et al. 2014. The bathymetry was derived from data made available by the Southeastern Universities Research Association (SURA) Inundation Testbed. This is a high- (approx. 30-m) resolution dataset that covers much of the northern Gulf of Mexico. In the deeper water not covered by the SURA data, the bathymetry was obtained from the National Geophysical Data Center (NGDC) Coastal Relief Model, Shuttle Radar Topography Mission (SRTM) and from the General Bathymetric Chart of the Ocean (GEBCO).

The horizontal grid resolution for the Ike simulations is $0.02°$ (approximately 2 km). The grid size is 504×348 points in the x (longitude) and y (latitude) directions, respectively. Grid cells with an elevation less than $+10$ m were taken to be within the computational domain and, hence, subject to WAD. Grid cells with an elevation $\geq +10$ m were defined to be land points outside the computational domain. The model was run with one vertical layer. A quadratic form of the bottom drag was used (see Section 2.5), with a minimum bottom drag coefficient of 0.0025 and bottom roughness of 0.01 m. A third-order upwind scheme was used for momentum advection. The time step was 60 seconds. Tidal boundary conditions for the 8 main tidal constituents (K_1, O_1, P_1, Q_1, K_2, M_2, N_2, S_2) from the OSU $1/45°$ Gulf of Mexico database were applied at the open boundaries.

The atmospheric forcing was provided by Oceanweather Inc. (OWI) on a longitude-latitude grid covering the Gulf of Mexico with a spatial resolution of $0.02°$ and a temporal resolution of 15 minutes, and included atmospheric pressure and wind velocities. These fields were interpolated to the NCOM grid, and the winds were adjusted for land effects by employing a directional land-masking scheme (Veeramony et al. 2014; Westerink et al. 2008). Wind stresses were computed from the wind velocities using standard bulk formulas with the wind-stress drag coefficient C_d computed as $C_d = 0.00218$ for U_a greater than 1 m/s, $C_d = 0.00062 + 0.00156/U_a$ for U_a between 1 and 3 m/s, $C_d = 0.00114$ for U_a between 3 and 10 m/s, $C_d = 0.00049 + 0.000065U_a$ for U_a between 10 and 26 m/s, and $C_d = 0.00216$ for U_a greater than 26 m/s, where U_a is the wind speed in m/s (Xia et al. 2008).

The Ike simulations were started from rest at 12Z on September 5, 2008. This is well before Ike entered the Gulf of Mexico on September 9 and allows sufficient time for the model to spin-up before Ike enters the model domain. The model was run for 10 days from 12Z September 5 to 12Z September 15.
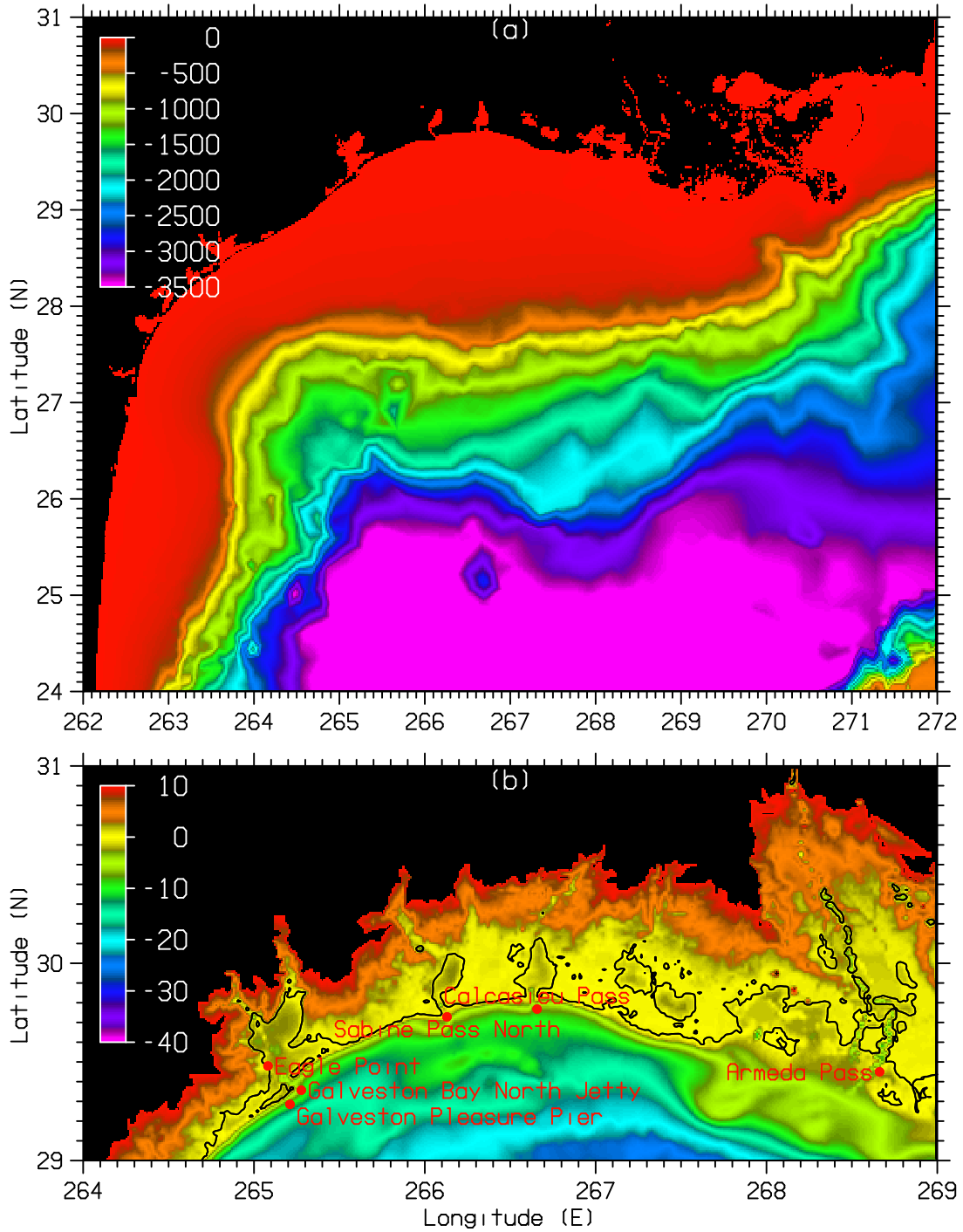
Fig. 18 — Upper plot (a) shows model domain and bathymetry (m) used for Hurricane Ike simulations. Contours are from -3500 to 0 m. Land elevations are not shown. Lower plot (b) shows bathymetry and land elevations (m) along a portion of the Texas and Louisiana coasts. Contours are from -40 to +10 m. The approximate coastline is shown by the black line. The locations of NOS tide stations used to validate the SSH predictions are indicated by red dots.
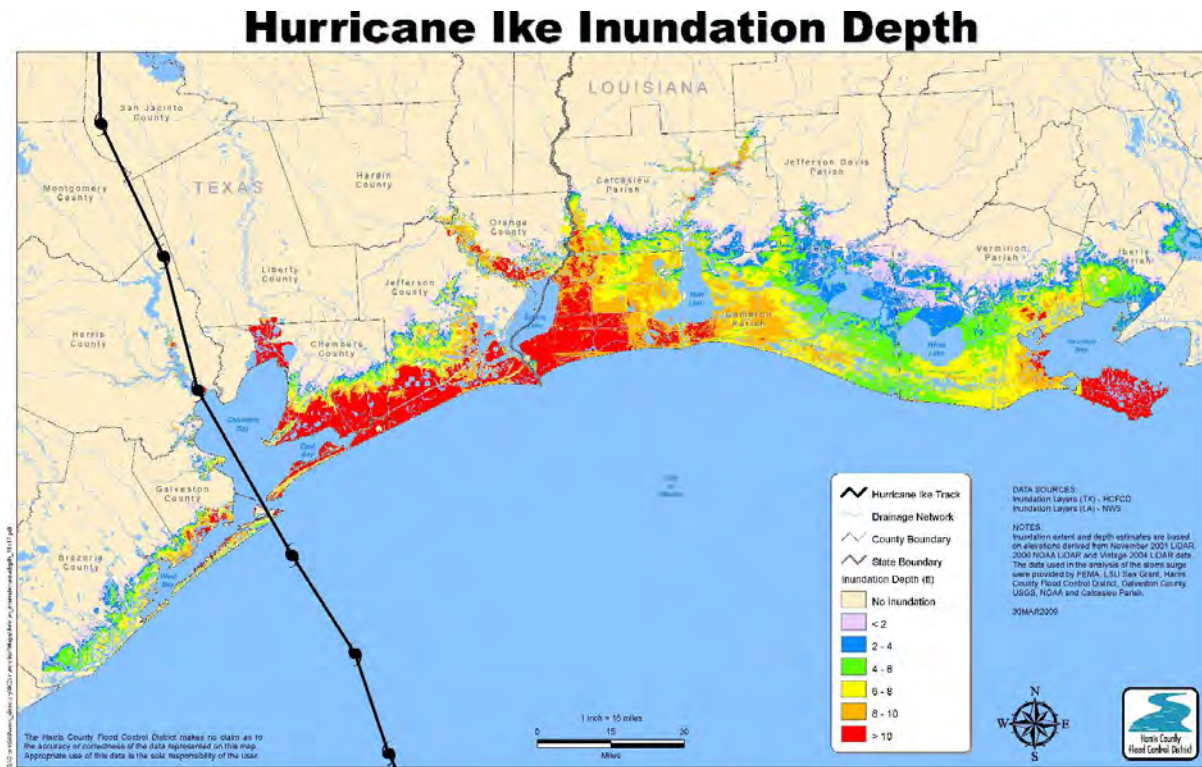
Fig. 19 — Hurricane Ike Inundation Map. (Obtained from Harris County Flood Control District *www.hcfcd.org*)

One of the most important aspects of a hurricane that people in the path of the storm would like to know is where and when flooding will occur due to the storm surge. The estimated inundation (depth of flooding) caused by Ike, as determined by the Harris County (Texas) Flood Control District, is shown in Fig. 19.

To qualitatively compare with the observed inundation map in Fig. 19, the maximum inundation from the NCOM simulation is shown in Fig. 20. The model results show areas of maximum inundation along the coast from Galveston Bay, TX to Mud Lake, LA. The inundation from the model simulation sometimes reaches further inland than the observed inundation in Figure 19. However, the magnitude of the observed inundation in Fig. 19 appears to be underestimated by the model simulation by a meter or more.

During Hurricane Ike, several National Ocean Service (NOS) tide stations along the Texas-Louisiana coast recorded the water levels as the storm made landfall. Figure 18b shows the locations of six NOS stations used to compare the observed water levels with the model results.

Figure 21 contains plots comparing the NOS observed water levels (black lines) with the NCOM simulated water levels (blue lines). In this figure, it can be seen that, up to September 9, the observed and simulated water levels are relatively close, with the model under-estimating the observed water levels by about 0.2 m. After September 9, as Ike begins to move closer to shore and affect the water levels near shore, the model water levels rise, but under-estimate the observed values by about a meter. One possible explanation for the under-estimation of the water levels is that the effect of waves on the water levels is not accounted for. Veeramony et al. (2014) found that the inclusion of wave processes increased the modeled water levels by an average of about 0.8 m (see
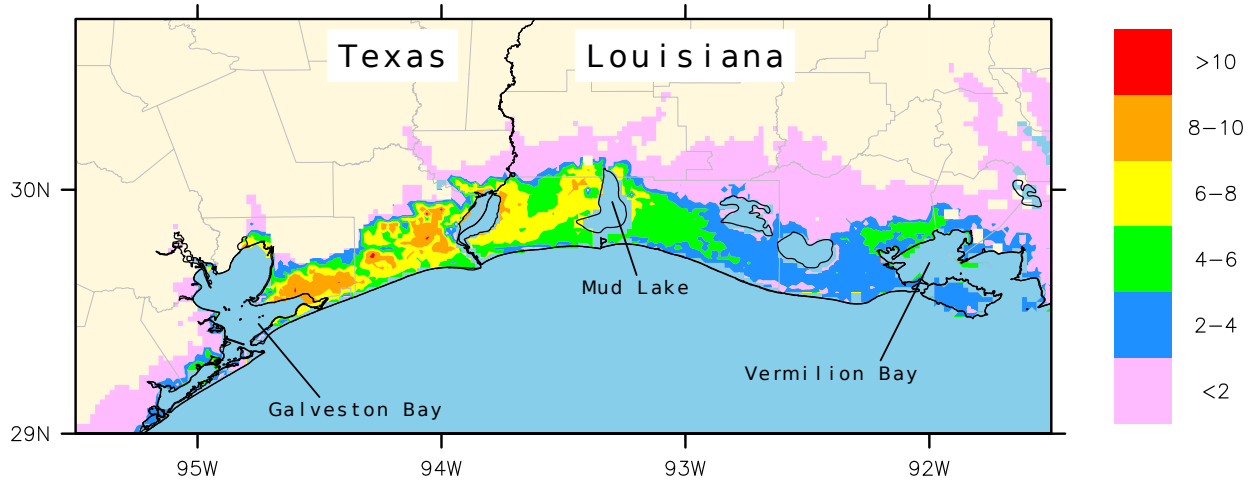
Fig. 20 — Maximum water inundations (m) from NCOM simulation.

their Fig. 2.1-15). If the inclusion of wave processes in NCOM resulted in a similar increase in the mean water levels, the comparison with the observed water levels would be significantly improved.

A baroclinic, multi-layer simulation of Hurricane Ike was run using a vertical grid with a total of 40 layers, with 19 sigma layers between the surface and the bottom down to a depth of -115 m and 21 fixed-depth levels between -115 m and -3500 m. Hence, the vertical grid in water shallower than -115 m, including the WAD areas, was 19 sigma layers. The maximum static surface layer thickness in deep water was 1 m and the grid was smoothly stretched in the vertical, with each layer being 17% thicker than the layer above. The horizontal grid and bathymetry were the same as used for the barotropic simulation (Fig. 18). The SSH, velocity, temperature, and salinity were initialized from operational Global NCOM fields obtained from the Naval Oceanographic Office (NAVO). The lateral boundary conditions consisted of tidal forcing as used for the barotropic simulation plus daily values of SSH, velocity, temperature, and salinity from Global NCOM. The surface atmospheric forcing was the surface pressure and wind stresses from Oceanweather Inc. as used for the barotropic simulation. The timestep used was 60 s, the same as for the barotropic simulation. This baroclinic, multi-layer, WAD simulation of Hurricane Ike ran smoothly. Figure 22 shows the model-predicted SST at 00Z September 14 after Ike had gone ashore near Galveston, TX. The SST shows surface cooling of up to 5°C along the track of the hurricane caused by upwelling and vertical mixing.

4. LIMITATIONS OF WAD IN NCOM

4.1 Time-Step Limitations

The WAD results in NCOM were not found to be very sensitive to the time step, despite that fact that a relatively large time step is used for the implicit solution of the barotropic mode in NCOM. This is probably because the WAD scheme in NCOM always maintains a minimum specified water depth D_{min} at all the grid cells within the computational domain. This avoids having to reduce the time step to prevent the water depth D from dropping from above D_{min} to
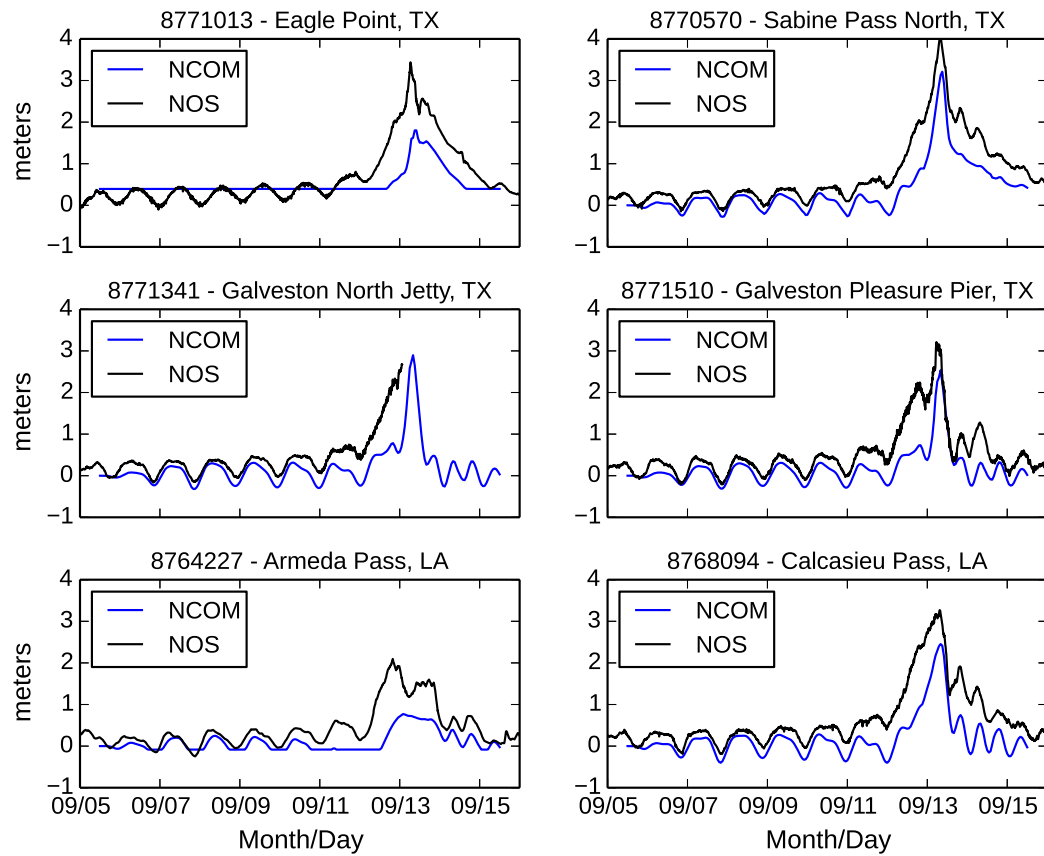
Fig. 21 — Observed NOS (black) and model-simulated (blue) water levels for Hurricane Ike. Note that the NOS gage at Galveston North Jetty stopped reporting values on September 13. The flat blue line at Eagle Point indicates that this area was dry in the model until September 13.
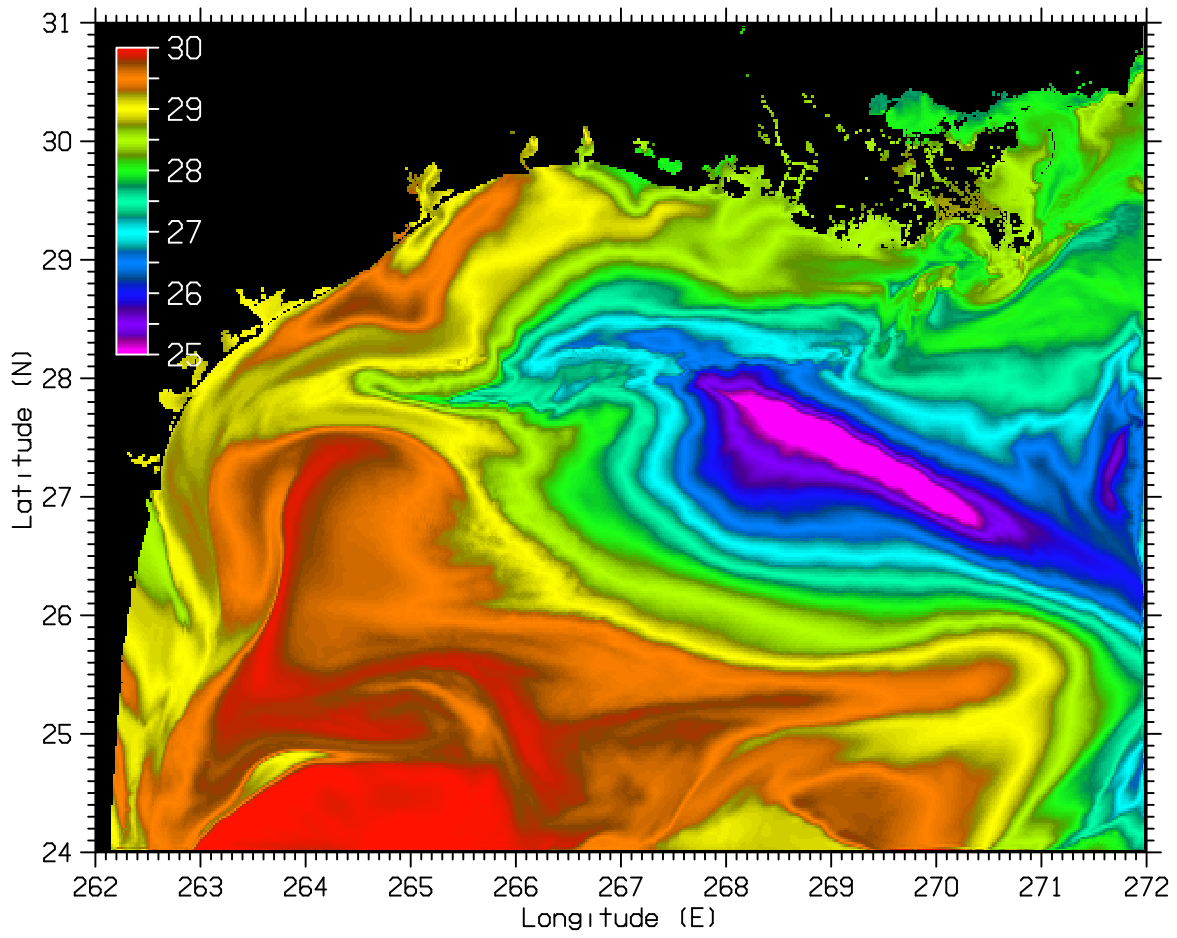
Fig. 22 — Model-simulated SST for Hurricane Ike at 00Z September 14, 2008 in °C.

below the bottom during a given time step. However, the use of a larger time step may increase the number of times the barotropic solver must be rerun during a single time step if there are extensive WAD areas. This is because, for a larger time step, there tend to be larger changes in the water depths for the WAD scheme to deal with.

However, the time step must be small enough to avoid exceeding the CFL constraints for advection. The occurrence of small water depths due to specifying a small value of D_{min} and the presence of relatively steep bottom slopes in WAD areas can both result in increased velocities that may require reduction of the time step to avoid exceeding the CFL limits for advection.

4.2 Bathymetry Limitations

There are no explicit limitations on the bathymetry for WAD in NCOM. However, as noted previously, the presence of steep bottom slopes can generate larger vertical velocities that may require a reduction of the time step to avoid violating the CFL constraint for vertical advection. Hence, having smooth changes in the bottom depth in WAD areas may allow the use of a larger time step and, consequently, reduce the run time.

4.3 WAD near Open Boundaries

At the present time, WAD cannot be handled at the open boundaries. Hence, a maximum allowable static bottom depth H must be specified at grid cells at open boundaries within the computational domain so WAD will not occur there. WAD at the open boundaries is currently being investigated in order to try to remove this restriction.

4.4 Effect of WAD on Run Time

The use of WAD in NCOM can increase the run time, both by increasing the time required during a single time step (due to the need to recompute the barotropic solver in NCOM a number of times during a single time step when there is WAD), and by increasing the number of time steps that are required (due to a need to decrease the time step to avoid violating the CFL constraints for advection).

The increase in the run time for "occasional" WAD, such as was used in the ChB simulations described in this report, tends to be small. As noted previously, "occasional" WAD refers to WAD that occurs only occasionally in a domain in which some maximum allowable static bottom depth H_{max}, with $H_{max} < 0$ (e.g., $H < H_{max} = -2$ m), has been prescribed for all the grid cells within the computational domain.

For "extensive" WAD, where there are extensive WAD areas and WAD is almost always occurring somewhere, such as in the SFB and CI simulations described in this report, the increase in the run time will tend to be more significant (due to the need to recompute the barotropic solver in NCOM a number of times during every, or almost every, time step). And as the grid resolution is increased in areas where there is "extensive" WAD, the increase in the run time needed for a single time step will tend to increase further.

5. SUMMARY

This report discusses the implementation and testing of wetting and drying (WAD) in the Navy Coastal Ocean Model (NCOM). NCOM is run as a stand-alone ocean model and also as part of the Coupled Ocean/Atmosphere Mesoscale Prediction System (COAMPS), which provides for one- or two-way coupling among atmosphere, ocean, and wave models.

The implementation of WAD in NCOM was complicated by the fact that NCOM uses an implicit numerical scheme to update the barotropic mode, i.e., to update the SSH and the depth-integrated transports. With the use of an implicit scheme to update the barotropic mode, the same, relatively large, timestep is used for the update of the barotropic mode that is used for the rest of the ocean model. This is possible because an implicit treatment of the barotropic mode is not limited by the speed of surface gravity waves, and so a much larger timestep can be used than if the barotropic mode were updated explicitly.

The WAD scheme is primarily implemented within NCOM's solution of the barotropic mode. After the new SSH is computed (using an iterative solver), the new water depth in each grid cell is inspected and, for grid cells whose depths have fallen below a prescribed minimum D_{min}, the volume fluxes at cell faces that are directed out of the drying grid cells are set to zero by setting the solver coefficient for those grid-cell faces to zero, and then the free-surface solver is rerun. This procedure is repeated until convergence occurs, i.e., until no grid-cell depths drop below D_{min} or the maximum difference in the SSH from the calculation of the SSH on the previous run of the solver falls below a small prescribed value. Hence, with this scheme, the water depth at grid cells within the computational domain is not allowed to fall much below the minimum specified depth D_{min}.

The WAD in NCOM was tested by running simulations of (a) idealized experiments that have expected or analytical solutions that can be compared against, (b) laboratory experiments that have observed results that can be compared against, (c) several coastal regions that have notable WAD areas, i.e., San Francisco Bay (SFB), Chesapeake Bay (ChB), and Cook Inlet in Alaska, and (d) Hurricane Ike, which caused extensive flooding along the Texas and Louisiana coasts in 2008.

The first of the idealized experiments consisted of a test of NCOM's horizontal symmetry when there are WAD areas within the domain and WAD is occurring. This is a test of NCOM's ability to exactly maintain a horizontally symmetric solution for a horizontally symmetric problem. This is one of the first tests conducted with NCOM after extensive changes have been made, since this type of test can detect many types of programming errors. NCOM maintained a perfectly symmetric solution for this test.

The second of the idealized tests consisted of the propagation of a planar surface wave rotating around within a parabolic-shaped basin. Wetting occurs at the leading edge of the wave as it propagates around the basin, and drying occurs at the trailing edge. The NCOM simulation was compared with the analytical solution. The NCOM solution agreed with the analytical solution, maintained the correct period of rotation of the wave around the basin, and maintained the amplitude of the wave for several revolutions with very little damping.

The first of the laboratory experiments consisted of a dam-break flow over a triangular bump. Water in a tank is released at the beginning of the experiment and flows down a channel in which

there is a triangular-shaped bump. Some of the water flows over the bump, and a surface wave is generated at the bump that propagates back towards the tank, reflects from the back wall of the tank, and propagates back towards the bump. This sequence is repeated several times until the surface wave propagating between the bump and the back of the tank is dissipated. The water height from the simulation was compared with the observed water height at seven different locations and the agreement was fairly good at all seven locations.

The second of the laboratory experiments consisted of a dam-break flow down a channel and around a 90° bend in the channel. At the bend, some of the water makes its way around the bend and some is reflected back towards the tank. The observed water height was measured during the experiment at six different locations, and the agreement between the simulated water height and the measured water height was fairly good at all of the locations.

The SFB simulations demonstrate that the WAD in NCOM can flood and drain extensive areas when used in different model configurations, including different grid resolutions (500, 200, and 100 m), in baroclinic or barotropic mode, with different numbers of layers (1–40), and with different numerical options.

The ChB case was run to illustrate the case of occasional WAD, where WAD occurs only occasionally due to drying of grid cells caused by very low tides and/or strong, offshore winds. Without a WAD capability, the drying out of grid cells caused NCOM to crash. With the WAD capability, NCOM continues to run smoothly when grid cells dry out. With just occasional WAD, there is no significant increase in the NCOM run time.

The Cook Inlet case demonstrates that the WAD scheme performs well in a region of very large (greater than 10 m) tidal range and extensive WAD areas. Cook Inlet has large areas of mud flats that are exposed at low tide. We focused on the tidal bore and flood that occurs in Turnagain Arm near the head of Cook Inlet. The eastern two-thirds of Turnagain Arm, which has a length of about 50 km, almost fully drains at low tide. The tidal bore that occurs when the tidal flood enters Turnagain Arm is a popular attraction; hence, the approximate arrival times of the bore at various locations along Turnagain Arm are well known. Initially, our simulated flood of Turnagain Arm occurred much later than observed. However, with improved bathymetry, we were able to achieve times that were much closer to the observed times.

The Hurricane Ike case demonstrates that the WAD performs well in high wind conditions in which the WAD is caused by large storm surge. However, the NCOM simulation underestimated the observed storm surge by about a meter. This underestimate may be due, at least in part, to the neglect of wave effects on the storm surge.

The pros and cons of the WAD scheme implemented in NCOM are discussed. The WAD scheme has the main advantages that it does not require any special modification of the bathymetry and is fairly robust. The main disadvantages of the WAD scheme are that (a) areas subject to WAD must be defined to be within the computational domain at the start of the simulation, (b) a minimum thickness of fluid must exist at all times within the WAD areas, i.e., the WAD areas can never be totally dry, and (c) additional calculations are required for the WAD and the timestep may need to be decreased, both of which increase the NCOM run time.

6. ACKNOWLEDGMENTS

7. REFERENCES

Alcrudo, F. (1999). Dambreak flow simulation with structured grid algorithms, in Proceedings of the CADAM meeting Wallingford, United Kingdom, 2–3 March 1998, edited by M. Morris, J.C. Galland, and P. Balabanis, European Commission, Rue de la Loi/Wetstraat 200, B-1049 Brussels, Belgium, 47–62.

Alcrudo, F., and S. Soares-Frazao (1999). Conclusions from the 1st CADAM Meeting – Wallingford, U.K., in Proceedings of the CADAM meeting Wallingford, United Kingdom, 2–3 March 1998, edited by M. Morris, J.C. Galland, and P. Balabanis, European Commission, Rue de la Loi/Wetstraat 200, B-1049 Brussels, Belgium, 35–46.

Allard, R., E. Rogers, P. Martin, T. Jensen, P. Chu, T. Campbell, J. Dykes, T. Smith, J. Choi, and U. Gravoisi (2014). The US Navy coupled ocean-wave prediction system, *Oceanography*, **27**(3), 92–103.

Barron, C.N., A.B. Kara, H.E. Hurlburt, C. Rowley, and L.F. Smedstad (2004). Sea Surface Height Predictions from the Global Navy Coastal Ocean Model (NCOM) During 1998–2001, *J. Atmos. Oceanic Technol.*, **21**(12), 1876–1894.

Benkhaldoun, F., L. Monthe, and I. Elmahi (1999). A splitting finite volume Roe scheme for shallow water equations with source terms, in Proceedings of the CADAM meeting Wallingford, United Kingdom, 2–3 March 1998, edited by M. Morris, J.C. Galland, and P. Balabanis, European Commission, Rue de la Loi/Wetstraat 200, B-1049 Brussels, Belgium, 63–88.

Biscarini C., S. Di Francesco, and P. Manciola (2010). CFD modelling approach for dam break flow studies, *Hydrol. Earth Syst. Sci.*, **14**, 705–718.

Blumberg, A.F., and G.L. Mellor (1987). A description of a three-dimensional coastal ocean circulation model, in *Three-Dimensional Coastal Ocean Models*, edited by N. Heaps, American Union, New York, 208 pp.

Brufau P., M.E. Vazquez-Cendon, and P. Garcia-Navarro (2002). Numerical model for the flooding and drying of irregular domains, *Int. J. Numer. Meth. Fluids*, **39**, 247–275.

Cozzolino, L., and D. Pianese (2006). High-order finite-volume modelling of one-dimensional flows, in *River Flow 2006*, 493–502, edited by Ferreira, Alves, Leal, and Cardoso, Taylor and Francis Group, London, ISBN 0-415-40815-06.

Egbert, G.D., and S.Y. Erofeeva (2003). Efficient inverse modeling of barotropic ocean tides, *J. Atmos. Oceanic Tech.*, **19**, 183–204.

Ezer, T., and H. Liu (2009). Combining remote sensing data and an inundation model to map tidal mudflat regions and improve flood predictions: A proof of concept demonstration in Cook Inlet, Alaska, *Geophys. Res. Let.*, **36**, L04605, doi:10.29/2008GL036873.

Ezer, T., and H. Liu (2010). On the dynamics and morphology of extensive tidal mudflats: Integrating remote sensing data with an inundation model of Cook Inlet, Alaska, *Ocean Dyn.*, **60**, 1307–1318. doi:10.1007/s10236-010-0319-x.

Garcia-Navarro, P., and P. Brufau (1999). One dimensional dambreak flow modelling: some results, in Proceedings of the CADAM meeting Wallingford, United Kingdom, 2–3 March 1998, edited by M. Morris, J.C. Galland, and P. Balabanis, European Commission, Rue de la Loi/Wetstraat 200, B-1049 Brussels, Belgium, 101–114.

Guan, M., N.G. Wright, and P.A. Sleigh (2013). Robust 2D shallow water model for solving flow over complex topography using homogeneous flux method, *Int. J. Num. Meth. Fluids*, **73**, 225–249.

Holland, W.R., J.C. Chow, and F.O. Bryan (1998). Application of a third-order-upwind scheme in the NCAR Ocean Model, *J. Clim.*, **11**, 1487–1493.

Khan, A.A., and W. Lai (2014). *Modeling Shallow-Water Flows Using the Discontinuous Galerkin Method*. CRC Press, Taylor and Francis Group, 6000 Broken Sound Parkway NW, Suite 300, Boca Raton, FL, 215 pp.

Kowalik, A., and A. Proshutinsky (2010). Tsunami–tide interactions: A Cook Inlet case study, *Cont. Shelf Res.*, **30**, 633–642.

Liang, Q. and F. Marche (2009). Numerical resolution of well-balanced shallow-water equations with complex source terms, *Adv. Water Res.*, **32**, 873–884.

Loukili, Y., and A. Soulaimani (2007). Numerical tracking of shallow-water waves by the unstructured finite-volume WAF approximation, *Int. J. Comp. Meth. in Eng. Sci. and Mech.*, **9**, 1–14.

Martin, P.J. (1999). An ocean model applied to the Chesapeake Bay plume, Estuarine and Coastal Modeling, Proceedings of the 6th International Conference, edited by M.L. Spaulding and H.L. Butler, American Society of Civil Engineers, Reston, VA, 1055–1067.

Martin, P.J. (2000). A Description of the Navy Coastal Ocean Model Version 1.0, NRL Report NRL/FR/7322–00-9962, Naval Research Laboratory, SSC, MS 39529, 42 pp.

Matthews, J.B., and J.C.H. Mungall (1972). A numerical tidal model and its application to Cook Inlet, Alaska, *J. Mar. Res.*, **15**, 27–38.

Morey, S.L., P.J. Martin, J.J. O'Brien, A.A. Wallcraft, and J. Zavala-Hidalgo (2003). Export Pathways for River Discharged Fresh Water in the Northern Gulf of Mexico, *J. Geophys. Res.*, **108**, 1–15.

Morris M. (2000). CADAM: Concerted Action on Dam Break Modeling – Final Report, Report SR 571, HR Wallingford Limited, HR Wallingford.

Oey, L.-Y. (2005). A wetting and drying scheme for POM, *Ocean Modeling*, **9**, 133–150.

Oey, L.-Y. (2006). An OGCM with movable land-sea boundaries, *Ocean Modeling*, **13**, 176–195.

Oey, L.-Y., T. Ezer, C. Hu, and F.E. Muller-Karger (2007). Baroclinic tidal flows and inundation processes in Cook Inlet, Alaska: numerical modeling and satellite observations, *Ocn. Dyn.*, **57**, 205–221.

Ralson, D., and M. Stacey (2007). Tidal and meteorological forcing of sediment transport in tributary mudflat channels, *Cont. Shelf Res*, **27**, 1510–1527.

Singh, J., M.S. Altinakar, and Y. Ding (2011). Two-dimensional numerical modeling of dam-break flows over natural terrain using a central explicit scheme, *Adv. Water Res.*, **34**(10), 1366–1375.

Soares-Frazao, S., and F. Alcrudo (1999). Conclusions from the 3rd meeting of the IAHR working group on dambreak modelling, in Proceedings of the CADAM meeting Wallingford, United Kingdom, 2–3 March 1998, edited by M. Morris, J.C. Galland, and P. Balabanis, European Commission, Rue de la Loi/Wetstraat 200, B-1049 Brussels, Belgium, 27–34.

Soares Frazao, S., X. Sillen, and Y. Zech (1999). Dam-break flow through sharp bends: Physical model and 2D Boltzmann model validation, in Proceedings of the CADAM meeting Wallingford, United Kingdom, 2–3 March 1998, edited by M. Morris, J.C. Galland, and P. Balabanis, European Commission, Rue de la Loi/Wetstraat 200, B-1049 Brussels, Belgium, 151–170.

Soares-Frazao, S., and Zech (2002). Dam Break in channels with 90° bend, *J. Hydraul. Eng. ASCE*, **128**(11), 956–968.

Stroup, E.D., and R.J. Lynn (1963). *Atlas of Salinity and Temperature Distributions in Chesapeake Bay 1952-1961 and Seasonal Averages 1949-1961*, Report 63-1, Chesapeake Bay Institute, John Hopkins University, 410 pp.

Thacker W. (1981). Some exact solutions to the nonlinear shallow-water wave equations, *J. Fluid Mech.*, **107**, 499–508.

Valle-Levinson, A., C. Li, T.C. Royer, and L.P. Atkinson (1998). Flow patterns at the Chesapeake Bay entrance, *Cont. Shelf Res.*, **18**, 1157–1177.

Veeramony, J., A. Condon, R. Linzell, and K. Watson (2014). Validation of Delft3D as a Coastal Surge and Inundation Prediction System, NRL Report NRL/MR/7320–2013-9495, Naval Research Laboratory, SSC, MS 39529, 126 pp.

Viseu, T., A. Bento Franco, A. Betamio de Almeida (1999). Numerical and computational results of the 2-D biplan model, in Proceedings of the CADAM meeting Wallingford, United Kingdom, 2–3 March 1998, edited by M. Morris, J.C. Galland, and P. Balabanis, European Commission, Rue de la Loi/Wetstraat 200, B-1049 Brussels, Belgium, 171–178.

Westerink, J.J., R.A. Luettich, J.C. Feyen, J.H. Atkinson, C. Dawson, H.J. Roberts, M.D. Powell, J.P. Dunion, E.J. Kubtatko, and H. Pourtaheri, 2008. A basin to channel scale unstructured grid hurricane storm surge model applied to southern Louisiana, *Mon. Wea. Rev.*, **136**, 833–864.

Xia, L., H. Liu, and M. Peng (2008). The effect of wave-current interactions on the storm surge and inundation in Charleston Harbor during Hurricane Hugo 1989, *Ocean Modelling*, **20**, 252–269.

Zimmermann, M., and M.M. Prescott (2014). Smooth Sheet Bathymetry of Cook Inlet, Alaska. U.S. Dep. Commer., NOAA Tech. Memo. NMFS-AFSC-275, 32 pp.